1 SARS-CoV-2 evolves increased infection elicited cell death and
2 fusion in an immunosuppressed individual

3

4

5 Gila Lustig[1]*, Yashica Ganga[2]*, Hylton Rodel[1,3], Houriiyah Tegally[4], Laurelle Jackson[2], Sandile

6 Cele[2,5], Khadija Khan[2,5], Zesuliwe Jule[2], Kajal Reedoy[2], Farina Karim[2,5], Mallory Bernstein[2],

7 Mahomed-Yunus S. Moosa[6], Derseree Archary[1], Tulio de Oliveira[4,7,8], Richard Lessells[4], Salim

8 S. Abdool Karim[1,9], Alex Sigal[1,2,5]

9

10 [1]Centre for the AIDS Programme of Research in South Africa, Durban, South Africa. [2]Africa Health
11 Research Institute, Durban, South Africa. [3]Division of Infection and Immunity, University College
12 London, London, UK. [4]KwaZulu-Natal Research Innovation and Sequencing Platform, Durban, South
13 Africa. [5]School of Laboratory Medicine and Medical Sciences, University of KwaZulu-Natal, Durban,
14 South Africa. [6]Department of Infectious Diseases, Nelson R. Mandela School of Clinical Medicine,
15 University of KwaZulu-Natal, Durban, South Africa. [7]Centre for Epidemic Response and Innovation
16 (CERI), School of Data Science and Computational Thinking, Stellenbosch University, Stellenbosch,
17 South Africa. [8]Department of Global Health, University of Washington, Seattle, USA. [9]Department of
18 Epidemiology, Mailman School of Public Health, Columbia University, New York, NY, United States.
19

20 *Equal contribution

21

22 **Abstract**

23

24 **The milder clinical manifestations of Omicron infection relative to pre-Omicron SARS-**

25 **CoV-2 raises the possibility that extensive evolution results in reduced pathogenicity.**

26 **To test this hypothesis, we quantified induction of cell fusion and cell death in SARS-**

27 **CoV-2 evolved from ancestral virus during long-term infection. Both cell fusion and**

28 **death were reduced in Omicron BA.1 infection relative to ancestral virus. Evolved virus**

29 **was isolated at different times during a 6-month infection in an immunosuppressed**

30 **individual with advanced HIV disease. The virus isolated 16 days post-reported**

31 **symptom onset induced fusogenicity and cell death at levels similar to BA.1. However,**

32 **fusogenicity was increased in virus isolated at 6 months post-symptoms to levels**

33 **intermediate between BA.1 and ancestral SARS-CoV-2. Similarly, infected cell death**

34 **showed a graded increase from earlier to later isolates. These results may indicate that,**

35 **at least by the cellular measures used here, evolution in long-term infection does not**

36 **necessarily attenuate the virus.**

37

38

Introduction

The reduced incidence of severe disease reported with Omicron[1] may result from the increasing immunity of the population because of vaccination and previous infections. Alternatively, the virus itself may have decreased its propensity to cause more severe disease[2-4]. If the ability of the Omicron virus itself to cause severe disease is attenuated independently of increased population immunity, the question arises of whether the virus is constrained to attenuate because of the evolutionary process through which variants emerge.

Mechanisms of variant formation may include reverse zoonosis[5-14], the infection of an animal reservoir where the virus mutates to adapt to the new host species, then re-infection of a human host, or evolution in long-term infection in immunosuppressed individuals[15-27]. Evolution in long-term infection in immunosuppression is documented to occur in some people who are immunosuppressed because of advanced HIV disease[15-17,26], defined as a CD4 T cell count < 200 cells/microliter in a person living with HIV.

Analysis of multiple long-term infections in immunosuppressed individuals has demonstrated recurrent mutations that are associated with escape from neutralizing antibodies[24]. However, mutations outside of spike are also common[28] and may affect virus infection and cell-cell spread and may therefore impact pathogenicity[24], with one possible outcome being that pathogenicity is reduced. In cell culture, viruses attenuate during long-term passaging, and such passaging is used to make live attenuated vaccines[29].

SARS-CoV-2 infection can lead to disease in several ways[30]. One hallmark is the presence in the lung of syncytia, cells which underwent fusion through the interaction of the SARS-CoV-2 spike protein expressed on the infected cell surface with the human angiotensin converting enzyme 2 (ACE2) receptor on neighbouring cells[31-34]. Fusion results in multinucleated cells. This phenotype can be readily reproduced in cell culture infection with SARS-CoV-2[35-38].

The sequence of events which leads to the ability of the virus to enter cells by binding ACE2 on the plasma membrane is also required for infected cells to efficiently fuse to other cells. SARS-CoV-2 spike has two subunits, S1 and S2. The S1 subunit binds the ACE2 receptor, while S2 mediates membrane fusion[39]. Spike contains an S1/S2 cleavage site predominantly cleaved by the cellular furin protease[32]. This cleavage allows further cleavage at the S2' site mediated by the cellular serine protease TMPRSS2, activating the S2 subunit for fusion[39]. A cathepsin-dependent alternate pathway for viral entry exists and enables TMPRSS2-independent viral infection[32]. The Omicron BA.1 subvariant does not have efficient S1/S2

2

76   cleavage and predominantly uses the alternative pathway to infect[31,40,41]. Consequently, cell-
77   cell fusion induced by BA.1 is lower than with ancestral SARS-CoV-2 and Delta variant
78   infections[31]. Generally, pre-Omicron variants show enhanced fusogenicity compared to
79   ancestral virus[42-45], while Omicron subvariants BA.1 and BA.2 show decreased fusogenicity
80   which correlates with decreased pathogenicity in hamster infections[31,44,46,47]. In the Omicron
81   BA.4 and BA.5 subvariants, fusogenicity is higher relative to BA.1 and BA.2[44,46], and this is
82   associated with higher pathogenicity in hamsters[46].

84   SARS-CoV-2 infection also leads to death of infected cells[48,49] which can be recapitulated in
85   cellular assays[50-52]. Cell death may initiate an inflammatory response and lead to the trafficking
86   of immune cells to the site of inflammation (reviewed in[53,54]). This causes increased lung fluid,
87   cellularity, and later scarring, and in turn leads to less oxygen being able to diffuse into the
88   blood, resulting in respiratory distress (reviewed in[55]). A reduction in cell death upon infection
89   would therefore be predicted to lead to lower levels of inflammation and therefore lower
90   disease severity.

92   We have previously reported on the evolution of SARS-CoV-2 from ancestral virus infection
93   in an individual who was immunosuppressed because of advanced HIV disease[15,16]. Here we
94   used timelapse microscopy and flow cytometry assays to determine changes in cell fusion and
95   cell death induced by SARS-CoV-2 as it evolves over half a year of continuous infection. As a
96   reference, we show cell fusion and cell death with Omicron BA.1 infection and ancestral virus
97   with the D614G substitution.

99   We observed that virus from relatively early in the infection induced cell fusion and death at
100   similar levels to Omicron BA.1. However, the virus which evolved over 6 months of infection
101   showed fusogenicity intermediate between BA.1 and D614G and cell death induction more
102   similar to D614G, indicating that, at least by these parameters, the virus did not attenuate
103   during the course of evolution.

105   **Results**

107   We isolated live virus from an individual with advanced HIV disease[15] (defined as CD4 T cell
108   count of less than 200 cells per microliter) who was enrolled in our longitudinal cohort to
109   investigate the immune response to SARS-CoV-2 infection. Participants in the study cohort
110   were sampled as soon as practicable post-diagnosis, then within the first month post-
111   diagnosis, and subsequently at 3-month intervals[56]. In the participant with advanced HIV,
112   continuous SARS-CoV-2 infection was detected by qPCR from combined nasopharyngeal and

3

113 oropharyngeal swabs for a period of 6 months from the date of diagnosis (Figure 1A), with
114 virus isolation performed from day 6 post-diagnosis (isolate designated D6), the first available
115 sample for isolation, up to day 190 post-diagnosis (designated D190). We have previously
116 sequenced these viral isolates and tested them for escape from neutralizing antibodies elicited
117 by SARS-CoV-2 infection[15]. D6 had low to moderate immune escape from plasma sampled
118 from convalescent individuals previously infected with either ancestral SARS-CoV-2, the Beta,
119 or the Delta variant. However, D190 showed more extensive immune escape from ancestral
120 virus and Delta variant infection elicited neutralizing antibodies (Figure 1B, modified analysis
121 with data from ref[15]). Phylogenetic analysis of the infection showed a pattern consistent with
122 the evolution of one ancestral virus infection (Figure 1C). Viral isolates D6, day 20 (D20), day
123 34 (D34), day 106 (D106) and D190 showed mutations in spike and other viral genes relative
124 to ancestral virus, with neutralization escape mutation E484K along with multiple other
125 mutations already present in D6 and the neutralization escape mutations K417T and F490S[57]
126 being present in the D190 isolate (Figure 1D).

127

128 To test whether the virus has evolved other changes in addition to neutralizing antibody
129 escape, we used the isolated viruses to infect the human H1299 lung cell line overexpressing
130 the ACE2 receptor[58]. All results reported here are from live virus infections. This cell line has
131 the endogenous histone H2AZ gene labelled with YFP by the insertion of the fluorophore
132 sequence as an artificial exon into the first intron[59], giving nuclear fluorescence. We used this
133 nuclear fluorescence signal combined with automated image analysis to detect fused cells
134 and cell number. We performed time-lapse microscopy with cells grown under controlled
135 temperature and CO_2 over 48 hours with images taken every 10 minutes. Uninfected cells
136 grew until confluence with little evidence of cell death and cell-cell fusion (Video 1). In contrast,
137 cells infected with an ancestral SARS-CoV-2 D614G isolate led to cell fusion, cell death and/or
138 lack of cell division which became apparent about 12 hours post-infection (Video 2). These
139 effects seemed less pronounced in cells infected with the Omicron BA.1 subvariant (Video 3)
140 and in the D6 isolate from early after diagnosis (Video 4). However, the D190 isolate from 6
141 months later seemed to have increased fusogenicity and cytotoxic/cytostatic effects relative
142 to BA.1 and D6 (Video 5).

143

144 We noted that cell nuclei become clustered together to form a contiguous region of
145 fluorescence during cell fusion (Figure 2A). We used an automated image analysis pipeline
146 (Figure 2 – figure supplement 1) to detect fused cells and cell number. Detection of fused cells
147 was based on the observation that in the absence of fusion, individual cell nuclei are distinct
148 even in confluent cell culture because they are separated by cellular cytoplasm. After fusion,

149   cell nuclei are close together and form an area considerably larger than a single nucleus

150   (Figure 2- figure supplement 1, Materials and methods).

151

152   Given that our image analysis pipeline was not designed to detect dead cells, we excluded

153   the last 12 hours of the movies when extensive cell death occurred. Quantifying fusions over

154   multiple independent experiments showed that uninfected cell culture had a low frequency of

155   fusions which did not increase over time. Infection by the D614G virus showed an increasing

156   fusion frequency, with about 40% of cell nuclei in fused cells by 36 hours post-infection. The

157   frequency of fusions was lower with BA.1 infection throughout and reached less than half of

158   that seen in the D614G infection. The pattern in D6 virus infections was similar to BA.1, while

159   with D190 the frequency of fusions was intermediate between BA.1 and D614G infection

160   (Figure 2B).

161

162   To quantify changes in cell number relative to the start of the movie, we used the number of

163   nuclei as a measure of cell number Cell numbers in uninfected cultures increased until they

164   were about 2.5-fold higher at 36 hours relative to the start of the movie. For the D614G

165   infection, cell numbers stopped increasing about 20 hours post-infection and started to

166   decrease. In BA.1 and D6 infection, the number of cells also stopped increasing after about

167   20 hours but did not decrease to the same extent as with ancestral virus. Infection with the

168   evolved D190 virus from late in the infection showed a similar but less pronounced decline in

169   cell numbers as D614G (Figure 2C). Excluding nuclei in fusions from the results gave a similar

170   pattern (Figure 2- figure supplement 2).

171

172   We used a second assay to detect cell death at 24 hours post-infection. We used this relatively

173   early timepoint because to avoid the effect of multiple infections per cell when infection is

174   saturating[60,61], which happens later (see for example Video 2). Infection was detected by

175   staining for SARS-CoV-2 nucleocapsid, and the fraction of dead infected cells determined by

176   co-staining with a death detection dye. The positive control was addition of ethanol (Figure

177   3A). We compared infection by ancestral virus to BA.1 and observed that, while the fraction of

178   infected cells was similar and slightly higher in BA.1 relative to ancestral virus, the fraction of

179   the infected cell population staining positive for the death detection dye was lower in BA.1

180   (Figure 3A).

181

182   We tested two independent isolates of ancestral D614G virus (D614G.1, D614G.2, see

183   Materials and methods), Omicron subvariants BA.1 and BA.5, the D6 and D190 isolates, and

184   isolates from study visits at day 20 (D20), 34 (D34), and 106 (D106) post-diagnosis. We then

185   calculated the ratio of the fraction of dead infected cells to total infected cells at 24 hours post-

186 infection. We observed that both isolates of ancestral virus caused cell death to a similar

187 extent, with about 11-13% of infected cells being detected as dead. The frequency of death

188 was about 3-fold lower for BA.1, at 4.2%, and was higher for BA.5, at 5.7%. The frequency of

189 D190 induced cell death, at 9.6%, was significantly higher than both BA.1 and BA.5 and more

190 like the ancestral virus isolates (Figure 3B). Among the isolates from the earlier timepoints,

191 D6 infection led to 5.6% dead infected cells, a similar frequency of cell death induction as

192 BA.5. The frequency of cell death increased to 6.8% for D20 and to 9.6% for D34 and D106.

193 The cell death frequency was significantly lower in D6 and D20 relative to D190 infections

194 (Figure 3C).

195

196 Because cell-cell fusion depends on cell surface spike expression, we investigated surface

197 spike expression on the infected cells in infection foci (where each focus contains on the order

198 of 10 cells, see[31]) formed by live virus on a confluent cell monolayer 18 hours post-infection.

199 To ensure that we did not inadvertently permeabilize the cells as part of the staining procedure,

200 thereby including intracellular spike, we also stained for SARS-CoV-2 nucleocapsid protein,

201 not present on the cell surface (Figure 4A). We observed that in unpermeabilized cells, surface

202 spike was readily detected. In contrast, nucleocapsid protein was not detected on the cell

203 surface, although levels were high after permeabilization. We then measured mean intensity,

204 which is independent of focus size, and normalized by the mean intensity of the ancestral

205 SARS-CoV-2 isolate (D614G isolate 1) included in each of the independent experiments. We

206 observed that the two ancestral virus isolates were similar in spike expression. BA.1 infection

207 showed significantly reduced cell surface spike, but levels increased moderately in BA.5

208 infection. D190 infection had significantly lower spike than the ancestral virus isolates but

209 higher surface spike relative to D6 infection (Figure 4B).

210

211 **Discussion**

212

213 Here we investigated the effect of evolutionary changes which happened in SARS-CoV-2 in

214 prolonged infection in an individual immunosuppressed because of advanced HIV disease.

215 We assayed a virus isolated from early in the course of infection at day 6 post-diagnosis, at

216 day 190 post-diagnosis, as well as at the intermediate timepoints. The day 6 isolate already

217 evolved a considerable number of mutations, or alternatively, the infecting virus was mutated.

218 Between day 6 and day 190 post-diagnosis, the infection evolved immune escape from

219 neutralizing antibodies, consistent with what is observed in long-term SARS-CoV-2 infections

220 in individuals with immunosuppression[24]. However, the ability of the virus to induce cell fusion

221 and cell death upon infection also changed through the course of evolution. While the early

222   viral isolate induced lower cell fusion and death compared to ancestral virus, induction of
223   fusion and cell death increased with evolution

225   We cannot determine whether the infecting virus evolved a reduced ability to cause cell fusion
226   and death by day 6 post-diagnosis, or whether this was a property of the infecting virus.
227   Symptom onset for the infection was reported to be 10 days pre-diagnosis[16], which a seems
228   a short time to evolve substantial differences relative to the ancestral virus, but we do not know
229   for certain how long the individual was infected. In addition, SARS-CoV-2 has been
230   documented to evolve relatively rapidly in some cases[62]. However, we have determined that
231   the subsequently isolated viruses evolved an enhanced ability to fuse cells and cause cell
232   death relative to the early isolate.

234   Consistent with the notion that highly mutated variants may not all have attenuated
235   pathogenicity, Beta variant infections in South Africa did not show lower pathogenicity relative
236   to ancestral virus infections[56]. This does not imply that there is no selective advantage in
237   attenuation. For example, variants which do not lead to more severe disease may be more
238   transmissible since the infected individual may continue daily activities and therefore transmit
239   to more people.

241   A possible selective pressure that results in the evolution of increased cell fusion is escape
242   from neutralizing antibodies. We and others have observed that cell-cell spread of SARS-CoV-
243   2 using this mechanism is insensitive to neutralizing antibodies, although inhibition is possible
244   at high antibody concentrations[43,63-65]. The immunosuppressed participant from whom the D6
245   and D190 viruses were isolated showed increasing neutralizing antibody activity during the
246   infection[15], and development of enhanced cell-cell spread may have been selected for to
247   escape neutralization. Higher infection elicited cell death may be related to increased
248   fusogenicity. This relationship seems to be present in the time-lapse data and is cell death,
249   and cell death because of syncytium formation is well characterized for HIV[66].

251   The Omicron subvariants circulating since November 2021 have led to infections with a lower
252   probability of developing severe disease[1,2,4,67]. Moreover, Omicron infection boosts the
253   immune response against other variants as well as against other Omicron subvariants[68], likely
254   maintaining protective immunity through infection. The results presented here, with the
255   limitations that we tested cellular parameters as measures of pathogenicity and viruses from
256   only one case of long-term evolution, may indicate that SARS-CoV-2 evolution in long-term
257   infection does not have to result in attenuation. It may indicate that a future variant could be
258   more pathogenic than currently circulating Omicron strains.

259

Materials and methods

261

<u>Informed consent and ethical statement</u>

Swabs for the isolation of ancestral (D614G.1 and D614G.2), Beta, Delta, D6, D20, D34, D106, and D190 viruses and blood samples to test virus neutralization were obtained after written informed consent from adults with PCR-confirmed SARS-CoV-2 infection who were enrolled in a prospective cohort study at the Africa Health Research Institute approved by the Biomedical Research Ethics Committee at the University of KwaZulu–Natal (reference BREC/00001275/2020). The Omicron/BA.1 was isolated from a residual swab sample with SARS-CoV-2 isolation from the sample approved by the University of the Witwatersrand Human Research Ethics Committee (HREC) (ref. M210752). The sample to isolate Omicron/BA.5 was collected after written informed consent as part of the COVID-19 transmission and natural history in KwaZulu-Natal, South Africa: Epidemiological Investigation to Guide Prevention and Clinical Care in the Centre for the AIDS Programme of Research in South Africa (CAPRISA) study and approved by the Biomedical Research Ethics Committee at the University of KwaZulu–Natal (reference BREC/00001195/2020, BREC/00003106/2021).

277

<u>Reagent availability statement</u>

Isolates and raw image files are available upon reasonable request. Sequences of isolated SARS-CoV-2 used in this study have been deposited in GISAID with accession:

281

Virus	GISAID number	PANGO
D614G.1	EPI_ISL_602626.1	B.1
D614G.2	EPI_ISL_602622	B.1.1.117
BA.1	EPI_ISL_7886688	BA.1
BA.5	EPI_ISL_12268493.2	BA.5
0027-D6	EPI_ISL_15541746	B.1.1.273
0027-D20	EPI_ISL_15541747	B.1.1.273
0027-D34	EPI_ISL_15541748	B.1.1.273
0027-D106	EPI_ISL_15541750	B.1.1.273
0027-D190	EPI_ISL_2397313	B.1.1.273

282

283

<u>Whole-genome sequencing, genome assembly and phylogenetic analysis</u>

8

285 RNA was extracted on an automated Chemagic 360 instrument, using the CMG-1049 kit
286 (Perkin Elmer, Hamburg, Germany). The RNA was stored at −80∘C prior to use. Libraries for
287 whole genome sequencing were prepared using either the Oxford Nanopore Midnight protocol
288 with Rapid Barcoding or the Illumina COVIDseq Assay. For the Illumina COVIDseq assay, the
289 libraries were prepared according to the manufacturer's protocol. Briefly, amplicons were
290 tagmented, followed by indexing using the Nextera UD Indexes Set A. Sequencing libraries
291 were pooled, normalized to 4 nM and denatured with 0.2 N sodium acetate. An 8 pM sample
292 library was spiked with 1% PhiX (PhiX Control v3 adaptor-ligated library used as a control).
293 We sequenced libraries on a 500-cycle v2 MiSeq Reagent Kit on the Illumina MiSeq
294 instrument (Illumina). On the Illumina NextSeq 550 instrument, sequencing was performed
295 using the Illumina COVIDSeq protocol (Illumina Inc, USA), an amplicon-based next-generation
296 sequencing approach. The first strand synthesis was carried using random hexamers primers
297 from Illumina and the synthesized cDNA underwent two separate multiplex PCR reactions.
298 The pooled PCR amplified products were processed for tagmentation and adapter ligation
299 using IDT for Illumina Nextera UD Indexes. Further enrichment and cleanup was performed
300 as per protocols provided by the manufacturer (Illumina Inc). Pooled samples were quantified
301 using Qubit 3.0 or 4.0 fluorometer (Invitrogen Inc.) using the Qubit dsDNA High Sensitivity
302 assay according to manufacturer's instructions. The fragment sizes were analyzed using
303 TapeStation 4200 (Invitrogen). The pooled libraries were further normalized to 4nM
304 concentration and 25 µL of each normalized pool containing unique index adapter sets were
305 combined in a new tube. The final library pool was denatured and neutralized with 0.2N sodium
306 hydroxide and 200 mM Tris-HCL (pH7), respectively. 1.5 pM sample library was spiked with
307 2% PhiX. Libraries were loaded onto a 300-cycle NextSeq 500/550 HighOutput Kit v2 and run
308 on the Illumina NextSeq 550 instrument (Illumina, San Diego, CA, USA). For Oxford Nanopore
309 sequencing, the Midnight primer kit was used as described by Freed and Silander55. cDNA
310 synthesis was performed on the extracted RNA using LunaScript RT mastermix (New England
311 BioLabs) followed by gene-specific multiplex PCR using the Midnight Primer pools which
312 produce 1200bp amplicons which overlap to cover the 30-kb SARS-CoV-2 genome.
313 Amplicons from each pool were pooled and used neat for barcoding with the Oxford Nanopore
314 Rapid Barcoding kit as per the manufacturer's protocol. Barcoded samples were pooled and
315 bead-purified. After the bead clean-up, the library was loaded on a prepared R9.4.1 flow-cell.
316 A GridION X5 or MinION sequencing run was initiated using MinKNOW software with the
317 base-call setting switched off. We assembled paired-end and nanopore.fastq reads using
318 Genome Detective 1.132 (https://www.genomedetective.com) which was updated for the
319 accurate assembly and variant calling of tiled primer amplicon Illumina or Oxford Nanopore
320 reads, and the Coronavirus Typing Tool56. For Illumina assembly, GATK HaploTypeCaller --
321 min-pruning 0 argument was added to increase mutation calling sensitivity near sequencing

322   gaps. For Nanopore, low coverage regions with poor alignment quality (<85% variant
323   homogeneity) near sequencing/amplicon ends were masked to be robust against primer drop-
324   out experienced in the Spike gene, and the sensitivity for detecting short inserts using a region-
325   local global alignment of reads, was increased. In addition, we also used the wf_artic (ARTIC
326   SARS-CoV-2) pipeline as built using the nextflow workflow framework57. In some instances,
327   mutations were confirmed visually with .bam files using Geneious software V2020.1.2
328   (Biomatters). The reference genome used throughout the assembly process was
329   NC_045512.2 (numbering equivalent to MN908947.3). For lineage classification, we used the
330   widespread dynamic lineage classification method from the 'Phylogenetic Assignment of
331   Named Global Outbreak Lineages' (PANGOLIN) software suite (https://github.com/hCoV-
332   2019/pangolin).

333

334   Cells
335   The H1299-E3 (H1299-ACE2, clone E3, H1299 originally from ATCC as CRL-5803) cell line
336   was derived from H1299 as described in our previous work[58,69]. The H1299-E3 cells were
337   propagated in growth medium consisting of complete Roswell Park Memorial Institute (RPMI)
338   1640 medium with 10% fetal bovine serum (Hyclone) containing 10mM of
339   hydroxyethylpiperazine ethanesulfonic acid (HEPES), 1mM sodium pyruvate, 2mM L-
340   glutamine and 0.1mM nonessential amino acids (all Sigma-Aldrich). Cells were passaged
341   every second day. For virus isolation, Vero E6 cells (originally ATCC CRL-1586, obtained from
342   Cellonex in South Africa) were propagated in complete growth medium consisting of
343   Dulbecco's Modified Eagle Medium (DMEM) with 10% fetal bovine serum (Hyclone) containing
344   10mM of HEPES, 1mM sodium pyruvate, 2mM L-glutamine and 0.1mM nonessential amino
345   acids (all Sigma-Aldrich). Vero E6 cells were passaged every 3–4 days.

346

347   Virus isolation
348   All work with live virus was performed in Biosafety Level 3 containment using protocols for
349   SARS-CoV-2 approved by the Africa Health Research Institute Biosafety Committee. ACE2-
350   expressing H1299-E3 cells were seeded at 4.5×10^5 cells in a 6 well plate well and incubated
351   for 18–20 h. After one Dulbecco's phosphate-buffered saline (DPBS) wash, the sub-confluent
352   cell monolayer was inoculated with 500 µL universal transport medium from swabs diluted 1:1
353   with growth medium filtered through a 0.45-µm filter. Cells were incubated for 1 h. Wells were
354   then filled with 3 mL complete growth medium. After 4 days of infection (completion of passage
355   1 (P1)), cells were trypsinized (Sigma-Aldrich), centrifuged at 300 rcf for 3 min and
356   resuspended in 4 mL growth medium. Then all infected cells were added to Vero E6 cells that
357   had been seeded at 1.5×10^5 cells per mL, 20 mL total, 18–20 h earlier in a T75 flask for cell-
358   to-cell infection. The coculture of ACE2-expressing H1299-E3 and Vero E6 cells was

359 incubated for 1 h and the flask was filled with 20 mL of complete growth medium and incubated

360 for 4 days. The viral supernatant from this culture (passage 2 (P2) stock) was used for

361 experiments.

362

363 Time-lapse microscopy

364 6-well glass bottom plates (MatTek) were coated with 300 µL of 0.001% fibronectin (Sigma-

365 Aldrich) in DPBS-/- (Gibco), incubated for 90 mins, then washed 3x with DPBS. H1299-E3

366 cells were then immediately plated at 60,000 cells per coated well. The next day the cells were

367 infected at 1000 focus-forming units in 1 mL growth media per well. Cell–virus mixtures were

368 incubated for 1 h at 37 °C, 5% CO_2 then an additional 1 mL of growth media was added.

369 Infections were imaged using a Metamorph controlled Nikon TiE motorized microscope (Nikon

370 Corporation) in a Biosafety Level 3 Facility with a 20x, 0.75 NA phase objective. Images were

371 captured using an 888 EMCCD camera (Andor). Temperature (37°C), humidity and CO_2 (5%)

372 were controlled using an environmental chamber (OKO Labs). Excitation source was 488 laser

373 line and emission was detected through a Semrock Brightline quad band 440–40 /521-21/607-

374 34/700-45 nm filter. For each well, 12 randomly chosen fields of view were captured every 10

375 minutes.

376

377 Image analysis

378 Timelapse microscopy images were analysed using custom MATLAB v.2019b (MathWorks)

379 script and using the MATLAB Image Analysis Toolbox. For each frame in the movie, both the

380 transmitted light and fluorescent images were used. A coarse segmentation was first

381 performed using the transmitted light image of the cells. Images were flatfield corrected and

382 contrast was enhanced by setting the top and bottom 1% of all pixel intensities to 1 and 0

383 respectively. The built-in function "rangefilt" was used to determine areas of high contrast

384 (where high pixel intensities were immediately adjacent to low pixel intensities) in the image

385 which corresponded to cell borders. Processed images were also median filtered and holes to

386 filled within segmented objects. The image was then thresholded to remove background signal

387 and obtain a mask of areas occupied by cells. The mask generated from the transmitted light

388 image was then used to remove objects that were not in areas occupied by cells. In the

389 fluorescence images corresponding to the transmitted light images. Fluorescence images

390 were then processed using flatfield correction, contrast enhancement and median filtering.

391 Fluorescent cell nuclei in the YFP channel were used to generate a binary mask for contiguous

392 objects in each image after thresholding. Each object was categorized as multi-nucleate or

393 uni-nucleate based on pixel area, where the threshold for a single nucleus was calculated as

394 the mean area of objects/nuclei in the uninfected condition, at 12 hours post-movie start, + 3

395 standard deviations of the mean. The fraction of cells in fusions was calculated by dividing the

11

396 total pixel area of objects above the single nucleus threshold by the total pixel area occupied

397 by nuclei in the same frame. The number of nuclei was calculated by dividing the total pixel

398 area occupied by nuclei by the mean pixel area of one nucleus in the uninfected condition at

399 12 hours post-movie start.

400

401 Detection of infected cell death

402 H1299-E3 cells were plated at 60,000 cells per well in 6-well plates (Corning) 1 day pre-

403 infection. The next day the cells were infected at 1000 focus-forming units in 1 mL growth

404 media per well. Cell–virus mixtures were incubated for 1 h at 37 °C, 5% CO_2 then an

405 additional 1 mL of growth media was added. 24 hours post-infection, cells were trypsinised

406 (Sigma-Aldrich), collected and stained with Blue Live/Dead stain as per manufacturer

407 instructions (L34961, ThermosScientific). The samples were then washed in 1 mL PBS-/-

408 and resuspended in Cytofix/Cytoperm (BD Biosciences) for 20 min at 4ºC in the dark. The

409 samples were then stained with 0.5 µg/mL anti-SARS-CoV-2 nucleocapsid-PE (ab283244,

410 Abcam) for 1 hour at 4ºC in the dark. Cells were analysed on an Aria Fusion (BD). Data was

411 analysed using FlowJo and Graphpad Prism 9.4.1 software.

412

413

414

415 Staining for cell-surface and total spike in a focus forming assay

416 H1299-E3 cells were plated in a 96-well plate (Corning) at 20,000 cells per well 1 day pre-

417 infection. Virus stocks were used at 100 focus-forming units per microwell. Cells were infected

418 with 100 µL of the virus for 1 h, then 100 µL of a 1X RPMI 1640 (Sigma-Aldrich, R6504), 1.5%

419 carboxymethylcellulose (Sigma-Aldrich, C4888) overlay was added without removing the

420 inoculum. Cells were fixed at 18 hours post-infection using 4% methanol-free formaldehyde

421 (ThermoScientific) for 20 minutes. For staining of foci, a rabbit anti-SARS-CoV-2 spike

422 monoclonal antibody (mAb BS-R2B12, GenScript A02058) at 0.5 ug/mL or a rabbit anti-

423 SARS-CoV-2 nucleocapsid monoclonal (ab271180 Abcam) at 1 ug/mL were used as the

424 primary detection antibody. Antibody was resuspended in either a permeabilization buffer

425 containing 0.1% saponin (Sigma-Aldrich), 0.1% BSA (Sigma-Aldrich), and 0.05% Tween-20

426 (Sigma-Aldrich) in PBS+/+ or a non-permeabilization buffer containing 0.1% BSA and 0.05%

427 Tween-20 in PBS+/+. Plates were incubated with primary antibody at room temperature for 2

428 hr with shaking, then washed with wash buffer containing 0.05% tween in PBS+/+. Secondary

429 goat anti-rabbit horseradish peroxidase (Abcam ab205718) was added at 1 ug/mL in either

430 permeabilization or non-permeabilization buffers as described above and incubated for 2

431 hours at room temperature with shaking. TrueBlue peroxidase substrate (SeraCare 5510-

432 0030) was then added at 50uL per well and incubated for 15 minutes at room temperature.

433 Plates were washed in distilled water and then dried for 2 hours and imaged in an ImmunoSpot

434 Ultra-V S6-02-6140 Analyzer ELISPOT instrument with BioSpot Professional built-in image

435 analysis (C.T.L). Data was analyzed using Graphpad Prism 9.4.1.

436

437 <u>Statistics and fitting</u>

438 Fitting was performed using MATLAB v.2019b. Neutralization data were fit to:

439

440 $Tx=1/(1+(D/ID_{50}))$.   (1)

441

442 Here Tx is the number of foci normalized to the number of foci in the absence of plasma on

443 the same plate at dilution D and ID_{50} is the plasma dilution giving 50% neutralization. $FRNT_{50}$

444 $= 1/ID_{50}$. Values of $FRNT_{50}$ <1 are set to 1 (undiluted), the lowest measurable value. We note

445 that the most concentrated plasma dilution was 1:25 and therefore $FRNT_{50}$ < 25 were

446 extrapolated. Fold-change was calculated by dividing the $FRNT_{50}$ obtained for the homologous

447 virus (the virus which elicited the immunity, e.g. D614G) by the $FRNT_{50}$ heterologous virus

448 (e.g. D190) per participant, then calculating the geometric mean and 95% confidence intervals

449 over all participant values. The 95% confidence intervals on the median in the time-lapse

450 microscopy data was calculated by first ranking the values in ascending order, then finding

451 the ranks of the lower and upper confidence interval by:

452

453 $LR = n/2-1.96\sqrt{(n/4)}$.   (2)

454 $UR = n/2+1.96\sqrt{(n/4)}$.   (3)

455

456 Here LR is lower 95% interval index in the ranked vector, UR is the upper 95% interval index

457 in the ranked vector. Values at indexes LR and UR were the lower 95% and upper 95%

458 confidence intervals, respectively. Other statistical tests, measures of central tendency and

459 confidence intervals were performed in GraphPad Prism version 9.4.1.

460

461

462 <u>Acknowledgements</u>

467

468 <u>Competing interest statement</u>

13

469   AS received an honorarium for a talk given to Pfizer employees.

470

471

472

473

474

475

476

477

478   **References**

479

480   1   Sigal, A., Milo, R. & Jassat, W. Estimating disease severity of Omicron and
481   Delta SARS-CoV-2 infections. *Nat Rev Immunol* **22**, 267-269 (2022).
482   PMC9002222. 10.1038/s41577-022-00720-5
483

484   2   Sigal, A. Milder disease with Omicron: is it the virus or the pre-existing
485   immunity? *Nature Reviews Immunology* **22**, 69-71 (2022). 10.1038/s41577-
486   022-00678-4
487

488   3   Whitaker, M., Elliott, J., Bodinier, B., Barclay, W., Ward, H., Cooke, G.,
489   Donnelly, C. A., Chadeau-Hyam, M. & Elliott, P. Variant-specific symptoms of
490   COVID-19 in a study of 1,542,510 adults in England. *Nat Commun* **13**, 6856
491   (2022). PMC9651890. 10.1038/s41467-022-34244-2
492

493   4   Ward, I. L., Bermingham, C., Ayoubkhani, D., Gethings, O. J., Pouwels, K. B.,
494   Yates, T., Khunti, K., Hippisley-Cox, J., Banerjee, A., Walker, A. S. & Nafilyan,
495   V. Risk of covid-19 related deaths for SARS-CoV-2 omicron (B.1.1.529)
496   compared with delta (B.1.617.2): retrospective cohort study. *Bmj* **378**,
497   e070695 (2022). PMC9344192. 10.1136/bmj-2022-070695
498

499   5   Griffin, B. D., Chan, M., Tailor, N., Mendoza, E. J., Leung, A., Warner, B. M.,
500   Duggan, A. T., Moffat, E., He, S., Garnett, L., Tran, K. N., Banadyga, L.,
501   Albietz, A., Tierney, K., Audet, J., Bello, A., Vendramelli, R., Boese, A. S.,
502   Fernando, L., Lindsay, L. R., Jardine, C. M., Wood, H., Poliquin, G., Strong, J.
503   E., Drebot, M., Safronetz, D., Embury-Hyatt, C. & Kobasa, D. SARS-CoV-2
504   infection and transmission in the North American deer mouse. *Nat Commun*
505   **12**, 3612 (2021). PMC8203675. 10.1038/s41467-021-23848-9
506

507   6   Meekins, D. A., Gaudreault, N. N. & Richt, J. A. Natural and Experimental
508   SARS-CoV-2 Infection in Domestic and Wild Animals. *Viruses* **13** (2021).
509   PMC8540328. 10.3390/v13101993
510

511   7   Kuchipudi, S. V., Surendran-Nair, M., Ruden, R. M., Yon, M., Nissly, R. H.,
512   Vandegrift, K. J., Nelli, R. K., Li, L., Jayarao, B. M., Maranas, C. D., Levine,
513   N., Willgert, K., Conlan, A. J. K., Olsen, R. J., Davis, J. J., Musser, J. M.,
514   Hudson, P. J. & Kapur, V. Multiple spillovers from humans and onward

515   transmission of SARS-CoV-2 in white-tailed deer. *Proc Natl Acad Sci U S A*
516   **119** (2022). PMC8833191. 10.1073/pnas.2121644119
517

518   8   Hale, V. L., Dennis, P. M., McBride, D. S., Nolting, J. M., Madden, C., Huey,
519   D., Ehrlich, M., Grieser, J., Winston, J., Lombardi, D., Gibson, S., Saif, L.,
520   Killian, M. L., Lantz, K., Tell, R. M., Torchetti, M., Robbe-Austerman, S.,
521   Nelson, M. I., Faith, S. A. & Bowman, A. S. SARS-CoV-2 infection in free-
522   ranging white-tailed deer. *Nature* **602**, 481-486 (2022). PMC8857059.
523   10.1038/s41586-021-04353-x
524

525   9   Koeppel, K. N., Mendes, A., Strydom, A., Rotherham, L., Mulumba, M. &
526   Venter, M. SARS-CoV-2 Reverse Zoonoses to Pumas and Lions, South
527   Africa. *Viruses* **14** (2022). PMC8778549. 10.3390/v14010120
528

529   10   Fenollar, F., Mediannikov, O., Maurin, M., Devaux, C., Colson, P., Levasseur,
530   A., Fournier, P. E. & Raoult, D. Mink, SARS-CoV-2, and the Human-Animal
531   Interface. *Front Microbiol* **12**, 663815 (2021). PMC8047314.
532   10.3389/fmicb.2021.663815
533

534   11   Bayarri-Olmos, R., Rosbjerg, A., Johnsen, L. B., Helgstrand, C., Bak-
535   Thomsen, T., Garred, P. & Skjoedt, M. O. The SARS-CoV-2 Y453F mink
536   variant displays a pronounced increase in ACE-2 affinity but does not
537   challenge antibody neutralization. *J Biol Chem* **296**, 100536 (2021).
538   PMC7948531. 10.1016/j.jbc.2021.100536
539

540   12   Hoffmann, M., Zhang, L., Krüger, N., Graichen, L., Kleine-Weber, H.,
541   Hofmann-Winkler, H., Kempf, A., Nessler, S., Riggert, J., Winkler, M. S.,
542   Schulz, S., Jäck, H. M. & Pöhlmann, S. SARS-CoV-2 mutations acquired in
543   mink reduce antibody-mediated neutralization. *Cell Rep* **35**, 109017 (2021).
544   PMC8018833. 10.1016/j.celrep.2021.109017
545

546   13   Ren, W., Lan, J., Ju, X., Gong, M., Long, Q., Zhu, Z., Yu, Y., Wu, J., Zhong,
547   J., Zhang, R., Fan, S., Zhong, G., Huang, A., Wang, X. & Ding, Q. Mutation
548   Y453F in the spike protein of SARS-CoV-2 enhances interaction with the mink
549   ACE2 receptor for host adaption. *PLoS Pathog* **17**, e1010053 (2021).
550   PMC8601601. 10.1371/journal.ppat.1010053
551

552   14   Zhou, J., Peacock, T. P., Brown, J. C., Goldhill, D. H., Elrefaey, A. M. E.,
553   Penrice-Randal, R., Cowton, V. M., De Lorenzo, G., Furnon, W., Harvey, W.
554   T., Kugathasan, R., Frise, R., Baillon, L., Lassaunière, R., Thakur, N., Gallo,
555   G., Goldswain, H., Donovan-Banfield, I., Dong, X., Randle, N. P., Sweeney,
556   F., Glynn, M. C., Quantrill, J. L., McKay, P. F., Patel, A. H., Palmarini, M.,
557   Hiscox, J. A., Bailey, D. & Barclay, W. S. Mutations that adapt SARS-CoV-2 to
558   mink or ferret do not increase fitness in the human airway. *Cell Rep* **38**,
559   110344 (2022). PMC8768428. 10.1016/j.celrep.2022.110344
560

561   15   Cele, S., Karim, F., Lustig, G., San, J. E., Hermanus, T., Tegally, H., Snyman,
562   J., Moyo-Gwete, T., Wilkinson, E., Bernstein, M., Khan, K., Hwa, S.-H., Tilles,
563   S. W., Singh, L., Giandhari, J., Mthabela, N., Mazibuko, M., Ganga, Y.,
564   Gosnell, B. I., Abdool Karim, S. S., Hanekom, W., Van Voorhis, W. C.,

15

565   Ndung'u, T., Lessells, R. J., Moore, P. L., Moosa, M.-Y. S., de Oliveira, T. &
566   Sigal, A. SARS-CoV-2 prolonged infection during advanced HIV disease
567   evolves extensive immune escape. *Cell Host & Microbe* (2022).
568   10.1016/j.chom.2022.01.005
569
570 16 Karim, F., Moosa, M. Y., Gosnell, B., Sandile, C., Giandhari, J., Pillay, S.,
571   Tegally, H., Wilkinson, E., San, E. J. & Msomi, N. Persistent SARS-CoV-2
572   infection and intra-host evolution in association with advanced HIV infection.
573   *medRxiv* (2021).
574 17 Riddell, A. C., Kele, B., Harris, K., Bible, J., Murphy, M., Dakshina, S., Storey,
575   N., Owoyemi, D., Pade, C., Gibbons, J. M., Harrington, D., Alexander, E.,
576   McKnight, Á. & Cutino-Moguel, T. Generation of novel SARS-CoV-2 variants
577   on B.1.1.7 lineage in three patients with advanced HIV disease. *Clin Infect Dis*
578   (2022). PMC9213850. 10.1093/cid/ciac409
579
580 18 Kemp, S. A., Collier, D. A., Datir, R. P., Ferreira, I., Gayed, S., Jahun, A.,
581   Hosmillo, M., Rees-Spear, C., Mlcochova, P., Lumb, I. U., Roberts, D. J.,
582   Chandra, A., Temperton, N., Collaboration, C.-N. B. C.-., Consortium, C.-G.
583   U., Sharrocks, K., Blane, E., Modis, Y., Leigh, K. E., Briggs, J. A. G., van Gils,
584   M. J., Smith, K. G. C., Bradley, J. R., Smith, C., Doffinger, R., Ceron-
585   Gutierrez, L., Barcenas-Morales, G., Pollock, D. D., Goldstein, R. A.,
586   Smielewska, A., Skittrall, J. P., Gouliouris, T., Goodfellow, I. G., Gkrania-
587   Klotsas, E., Illingworth, C. J. R., McCoy, L. E. & Gupta, R. K. SARS-CoV-2
588   evolution during treatment of chronic infection. *Nature* **592**, 277-282 (2021).
589   PMC7610568. 10.1038/s41586-021-03291-y
590
591 19 Peacock, T. P., Penrice-Randal, R., Hiscox, J. A. & Barclay, W. S. SARS-
592   CoV-2 one year on: evidence for ongoing viral adaptation. *The Journal of
593   General Virology* **102** (2021).
594 20 Jensen, B., Luebke, N., Feldt, T., Keitel, V., Brandenburger, T., Kindgen-
595   Milles, D., Lutterbeck, M., Freise, N., Schoeler, D. & Haas, R. Emergence of
596   the E484K mutation in SARS-COV-2-infected immunocompromised patients
597   treated with bamlanivimab in Germany. Lancet Reg Health Eur. 2021; 8:
598   100164. *J. LANEPE* (2021).
599 21 Baang, J. H., Smith, C., Mirabelli, C., Valesano, A. L., Manthei, D. M.,
600   Bachman, M. A., Wobus, C. E., Adams, M., Washer, L., Martin, E. T. &
601   Lauring, A. S. Prolonged Severe Acute Respiratory Syndrome Coronavirus 2
602   Replication in an Immunocompromised Patient. *J Infect Dis* **223**, 23-27
603   (2021). PMC7797758. 10.1093/infdis/jiaa666
604
605 22 Choi, B., Choudhary, M. C., Regan, J., Sparks, J. A., Padera, R. F., Qiu, X.,
606   Solomon, I. H., Kuo, H. H., Boucau, J., Bowman, K., Adhikari, U. D., Winkler,
607   M. L., Mueller, A. A., Hsu, T. Y., Desjardins, M., Baden, L. R., Chan, B. T.,
608   Walker, B. D., Lichterfeld, M., Brigl, M., Kwon, D. S., Kanjilal, S., Richardson,
609   E. T., Jonsson, A. H., Alter, G., Barczak, A. K., Hanage, W. P., Yu, X. G.,
610   Gaiha, G. D., Seaman, M. S., Cernadas, M. & Li, J. Z. Persistence and
611   Evolution of SARS-CoV-2 in an Immunocompromised Host. *N Engl J Med*
612   **383**, 2291-2293 (2020). PMC7673303. 10.1056/NEJMc2031364
613

23   Avanzato, V. A., Matson, M. J., Seifert, S. N., Pryce, R., Williamson, B. N., Anzick, S. L., Barbian, K., Judson, S. D., Fischer, E. R., Martens, C., Bowden, T. A., de Wit, E., Riedo, F. X. & Munster, V. J. Case Study: Prolonged Infectious SARS-CoV-2 Shedding from an Asymptomatic Immunocompromised Individual with Cancer. *Cell* **183**, 1901-1912.e1909 (2020). PMC7640888. 10.1016/j.cell.2020.10.049

24   Wilkinson, S. A. J., Richter, A., Casey, A., Osman, H., Mirza, J. D., Stockton, J., Quick, J., Ratcliffe, L., Sparks, N., Cumley, N., Poplawski, R., Nicholls, S. N., Kele, B., Harris, K., Peacock, T. P. & Loman, N. J. Recurrent SARS-CoV-2 mutations in immunodeficient patients. *Virus Evol* **8**, veac050 (2022). PMC9384748. 10.1093/ve/veac050

25   Maponga, T. G., Jeffries, M., Tegally, H., Sutherland, A., Wilkinson, E., Lessells, R. J., Msomi, N., van Zyl, G., de Oliveira, T. & Preiser, W. Persistent SARS-CoV-2 infection with accumulation of mutations in a patient with poorly controlled HIV infection. *Clin Infect Dis* (2022). PMC9278209. 10.1093/cid/ciac548

26   Hoffman, S. A., Costales, C., Sahoo, M. K., Palanisamy, S., Yamamoto, F., Huang, C., Verghese, M., Solis, D. C., Sibai, M. & Subramanian, A. SARS-CoV-2 Neutralization Resistance Mutations in Patient with HIV/AIDS, California, USA. *Emerging Infectious Diseases* **27** (2021).

27   Corey, L., Beyrer, C., Cohen, M. S., Michael, N. L., Bedford, T. & Rolland, M. SARS-CoV-2 Variants in Patients with Immunosuppression. *N Engl J Med* **385**, 562-566 (2021). PMC8494465. 10.1056/NEJMsb2104756

28   Kistler, K. E., Huddleston, J. & Bedford, T. Rapid and parallel adaptive mutations in spike S1 drive clade success in SARS-CoV-2. *Cell Host Microbe* **30**, 545-555.e544 (2022). PMC8938189. 10.1016/j.chom.2022.03.018

29   Lauring, A. S., Jones, J. O. & Andino, R. Rationalizing the development of live attenuated virus vaccines. *Nat Biotechnol* **28**, 573-579 (2010). PMC2883798. 10.1038/nbt.1635

30   Lamers, M. M. & Haagmans, B. L. SARS-CoV-2 pathogenesis. *Nature Reviews Microbiology* **20**, 270-284 (2022). 10.1038/s41579-022-00713-0

31   Meng, B., Abdullahi, A., Ferreira, I. A. T. M., Goonawardane, N., Saito, A., Kimura, I., Yamasoba, D., Gerber, P. P., Fatihi, S., Rathore, S., Zepeda, S. K., Papa, G., Kemp, S. A., Ikeda, T., Toyoda, M., Tan, T. S., Kuramochi, J., Mitsunaga, S., Ueno, T., Shirakawa, K., Takaori-Kondo, A., Brevini, T., Mallery, D. L., Charles, O. J., Baker, S., Dougan, G., Hess, C., Kingston, N., Lehner, P. J., Lyons, P. A., Matheson, N. J., Owehand, W. H., Saunders, C., Summers, C., Thaventhiran, J. E. D., Toshner, M., Weekes, M. P., Maxwell, P., Shaw, A., Bucke, A., Calder, J., Canna, L., Domingo, J., Elmer, A., Fuller, S., Harris, J., Hewitt, S., Kennet, J., Jose, S., Kourampa, J., Meadows, A., O'Brien, C., Price, J., Publico, C., Rastall, R., Ribeiro, C., Rowlands, J., Ruffolo, V., Tordesillas, H., Bullman, B., Dunmore, B. J., Fawke, S., Gräf, S., Hodgson, J., Huang, C., Hunter, K., Jones, E., Legchenko, E., Matara, C.,

17

664 Martin, J., Mescia, F., O'Donnell, C., Pointon, L., Shih, J., Sutcliffe, R., Tilly,
665 T., Treacy, C., Tong, Z., Wood, J., Wylot, M., Betancourt, A., Bower, G.,
666 Cossetti, C., De Sa, A., Epping, M., Fawke, S., Gleadall, N., Grenfell, R.,
667 Hinch, A., Jackson, S., Jarvis, I., Krishna, B., Nice, F., Omarjee, O., Perera,
668 M., Potts, M., Richoz, N., Romashova, V., Stefanucci, L., Strezlecki, M.,
669 Turner, L., De Bie, E. M. D. D., Bunclark, K., Josipovic, M., Mackay, M.,
670 Allison, J., Butcher, H., Caputo, D., Clapham-Riley, D., Dewhurst, E., Furlong,
671 A., Graves, B., Gray, J., Ivers, T., Le Gresley, E., Linger, R., Meloy, S.,
672 Muldoon, F., Ovington, N., Papadia, S., Phelan, I., Stark, H., Stirrups, K. E.,
673 Townsend, P., Walker, N., Webster, J., Scholtes, I., Hein, S., King, R.,
674 Butlertanaka, E. P., Tanaka, Y. L., Ikeda, T., Ito, J., Uriu, K., Kosugi, Y.,
675 Suganami, M., Oide, A., Yokoyama, M., Chiba, M., Motozono, C., Nasser, H.,
676 Shimizu, R., Yuan, Y., Kitazato, K., Hasebe, H., Nakagawa, S., Wu, J.,
677 Takahashi, M., Fukuhara, T., Shimizu, K., Tsushima, K., Kubo, H., Kazuma,
678 Y., Nomura, R., Horisawa, Y., Nagata, K., Kawai, Y., Yanagida, Y., Tashiro,
679 Y., Tokunaga, K., Ozono, S., Kawabata, R., Morizako, N., Sadamasu, K.,
680 Asakura, H., Nagashima, M., Yoshimura, K., Cárdenas, P., Muñoz, E.,
681 Barragan, V., Márquez, S., Prado-Vivar, B., Becerra-Wong, M., Caravajal, M.,
682 Trueba, G., Rojas-Silva, P., Grunauer, M., Gutierrez, B., Guadalupe, J. J.,
683 Fernández-Cadena, J. C., Andrade-Molina, D., Baldeon, M., Pinos, A.,
684 Bowen, J. E., Joshi, A., Walls, A. C., Jackson, L., Martin, D., Smith, K. G. C.,
685 Bradley, J., Briggs, J. A. G., Choi, J., Madissoon, E., Meyer, K., Mlcochova,
686 P., Ceron-Gutierrez, L., Doffinger, R., Teichmann, S. A., Fisher, A. J., Pizzuto,
687 M. S., de Marco, A., Corti, D., Hosmillo, M., Lee, J. H., James, L. C., Thukral,
688 L., Veesler, D., Sigal, A., Sampaziotis, F., Goodfellow, I. G., Matheson, N. J.,
689 Sato, K., Gupta, R. K., The, C.-N. B. C.-C., The Genotype to Phenotype
690 Japan Consortium, m. & Ecuador, C. C. Altered TMPRSS2 usage by SARS-
691 CoV-2 Omicron impacts tropism and fusogenicity. *Nature* (2022).
692 10.1038/s41586-022-04474-x
693
694 32 Hoffmann, M., Kleine-Weber, H. & Pöhlmann, S. A Multibasic Cleavage Site
695 in the Spike Protein of SARS-CoV-2 Is Essential for Infection of Human Lung
696 Cells. *Mol Cell* **78**, 779-784.e775 (2020). PMC7194065.
697 10.1016/j.molcel.2020.04.022
698
699 33 Papa, G., Mallery, D. L., Albecka, A., Welch, L. G., Cattin-Ortolá, J., Luptak,
700 J., Paul, D., McMahon, H. T., Goodfellow, I. G., Carter, A., Munro, S. &
701 James, L. C. Furin cleavage of SARS-CoV-2 Spike promotes but is not
702 essential for infection and cell-cell fusion. *PLoS Pathog* **17**, e1009246 (2021).
703 PMC7861537. 10.1371/journal.ppat.1009246
704
705 34 Cattin-Ortolá, J., Welch, L. G., Maslen, S. L., Papa, G., James, L. C. & Munro,
706 S. Sequences in the cytoplasmic tail of SARS-CoV-2 Spike facilitate
707 expression at the cell surface and syncytia formation. *Nat Commun* **12**, 5333
708 (2021). PMC8429659. 10.1038/s41467-021-25589-1
709
710 35 Buchrieser, J., Dufloo, J., Hubert, M., Monel, B., Planas, D., Rajah, M. M.,
711 Planchais, C., Porrot, F., Guivel-Benhassine, F., Van der Werf, S., Casartelli,
712 N., Mouquet, H., Bruel, T. & Schwartz, O. Syncytia formation by SARS-CoV-

713   2-infected cells. *Embo j* **39**, e106267 (2020). PMC7646020.
714   10.15252/embj.2020106267
715
716   36   Braga, L., Ali, H., Secco, I., Chiavacci, E., Neves, G., Goldhill, D., Penn, R.,
717   Jimenez-Guardeño, J. M., Ortega-Prieto, A. M., Bussani, R., Cannatà, A.,
718   Rizzari, G., Collesi, C., Schneider, E., Arosio, D., Shah, A. M., Barclay, W. S.,
719   Malim, M. H., Burrone, J. & Giacca, M. Drugs that inhibit TMEM16 proteins
720   block SARS-CoV-2 spike-induced syncytia. *Nature* **594**, 88-93 (2021).
721   PMC7611055. 10.1038/s41586-021-03491-6
722
723   37   Zhang, Z., Zheng, Y., Niu, Z., Zhang, B., Wang, C., Yao, X., Peng, H., Franca,
724   D. N., Wang, Y., Zhu, Y., Su, Y., Tang, M., Jiang, X., Ren, H., He, M., Wang,
725   Y., Gao, L., Zhao, P., Shi, H., Chen, Z., Wang, X., Piacentini, M., Bian, X.,
726   Melino, G., Liu, L., Huang, H. & Sun, Q. SARS-CoV-2 spike protein dictates
727   syncytium-mediated lymphocyte elimination. *Cell Death Differ* **28**, 2765-2777
728   (2021). PMC8056997. 10.1038/s41418-021-00782-3
729
730   38   Bussani, R., Schneider, E., Zentilin, L., Collesi, C., Ali, H., Braga, L., Volpe, M.
731   C., Colliva, A., Zanconati, F., Berlot, G., Silvestri, F., Zacchigna, S. & Giacca,
732   M. Persistence of viral RNA, pneumocyte syncytia and thrombosis are
733   hallmarks of advanced COVID-19 pathology. *EBioMedicine* **61**, 103104
734   (2020). PMC7677597. 10.1016/j.ebiom.2020.103104
735
736   39   Hoffmann, M., Kleine-Weber, H., Schroeder, S., Krüger, N., Herrler, T.,
737   Erichsen, S., Schiergens, T. S., Herrler, G., Wu, N. H., Nitsche, A., Müller, M.
738   A., Drosten, C. & Pöhlmann, S. SARS-CoV-2 Cell Entry Depends on ACE2
739   and TMPRSS2 and Is Blocked by a Clinically Proven Protease Inhibitor. *Cell*
740   **181**, 271-280.e278 (2020). PMC7102627. 10.1016/j.cell.2020.02.052
741
742   40   Peacock, T. P., Brown, J. C., Zhou, J., Thakur, N., Sukhova, K., Newman, J.,
743   Kugathasan, R., Yan, A. W. C., Furnon, W., De Lorenzo, G., Cowton, V. M.,
744   Reuss, D., Moshe, M., Quantrill, J. L., Platt, O. K., Kaforou, M., Patel, A. H.,
745   Palmarini, M., Bailey, D. & Barclay, W. S. The altered entry pathway and
746   antigenic distance of the SARS-CoV-2 Omicron variant map to separate
747   domains of spike protein. *bioRxiv*, 2021.2012.2031.474653 (2022).
748   10.1101/2021.12.31.474653
749
750   41   Willett, B. J., Grove, J., MacLean, O. A., Wilkie, C., De Lorenzo, G., Furnon,
751   W., Cantoni, D., Scott, S., Logan, N., Ashraf, S., Manali, M., Szemiel, A.,
752   Cowton, V., Vink, E., Harvey, W. T., Davis, C., Asamaphan, P., Smollett, K.,
753   Tong, L., Orton, R., Hughes, J., Holland, P., Silva, V., Pascall, D. J., Puxty, K.,
754   da Silva Filipe, A., Yebra, G., Shaaban, S., Holden, M. T. G., Pinto, R. M.,
755   Gunson, R., Templeton, K., Murcia, P. R., Patel, A. H., Klenerman, P.,
756   Dunachie, S., Dunachie, S., Klenerman, P., Barnes, E., Brown, A., Adele, S.,
757   Kronsteiner, B., Murray, S. M., Abraham, P., Deeks, A., Ansari, M. A., de
758   Silva, T., Turtle, L., Moore, S., Austin, J., Richter, A., Duncan, C., Payne, R.,
759   Ash, A., Koshy, C., Kele, B., Cutino-Moguel, T., Fairley, D. J., McKenna, J. P.,
760   Curran, T., Adams, H., Fraser, C., Bonsall, D., Fryer, H., Lythgoe, K.,
761   Thomson, L., Golubchik, T., Murray, A., Singleton, D., Beckwith, S. M.,
762   Mantzouratou, A., Barrow, M., Buchan, S. L., Reynolds, N., Warne, B.,

763   Maksimovic, J., Spellman, K., McCluggage, K., John, M., Beer, R., Afifi, S.,
764   Morgan, S., Mack, A., Marchbank, A., Price, A., Morriss, A., Bresner, C.,
765   Kitchen, C., Merrick, I., Southgate, J., Guest, M., Jones, O., Munn, R.,
766   Connor, T. R., Whalley, T., Workman, T., Fuller, W., Patel, A., Patel, B.,
767   Nebbia, G., Edgeworth, J., Snell, L. B., Batra, R., Charalampous, T., Beckett,
768   A. H., Shelest, E., Robson, S. C., Underwood, A. P., Taylor, B. E. W., Yeats,
769   C. A., Aanensen, D. M., Abudahab, K., Menegazzo, M., Joseph, A., Clark, G.,
770   Howson-Wells, H. C., Berry, L., Khakh, M., Lister, M. M., Boswell, T., Fleming,
771   V. M., Holmes, C. W., McMurray, C. L., Shaw, J., Tang, J. W., Fallon, K.,
772   Odedra, M., Willford, N. J., Bird, P. W., Helmer, T., Williams, L.-A., Sheriff, N.,
773   Campbell, S., Raviprakash, V., Blakey, V., Moore, C., Sang, F., Debebe, J.,
774   Carlile, M., Loose, M. W., Holmes, N., Wright, V., Torok, M. E., Hamilton, W.
775   L., Carabelli, A. M., Jermy, A., Blane, B., Churcher, C. M., Ludden, C.,
776   Aggarwal, D., Westwick, E., Brooks, E., McManus, G. M., Galai, K., Smith, K.,
777   Smith, K. S., Cox, M., Fragakis, M., Maxwell, P., Judges, S., Peacock, S. J.,
778   Feltwell, T., Kenyon, A., Eldirdiri, S., Davis, T., Taylor, J. F., Tan, N. K.,
779   Zarebski, A. E., Gutierrez, B., Raghwani, J., du Plessis, L., Kraemer, M. U. G.,
780   Pybus, O. G., Francois, S., Attwood, S. W., Vasylyeva, T. I., Jahun, A. S.,
781   Goodfellow, I. G., Georgana, I., Pinckert, M. L., Hosmillo, M., Izuagbe, R.,
782   Chaudhry, Y., Ryan, F., Lowe, H., Moses, S., Bedford, L., Cargill, J. S.,
783   Hughes, W., Moore, J., Stonehouse, S., Shah, D., Lee, J. C. D., Brown, J. R.,
784   Harris, K. A., Atkinson, L., Storey, N., Spyer, M. J., Flaviani, F., Alcolea-
785   Medina, A., Sehmi, J., Ramble, J., Ohemeng-Kumi, N., Smith, P., Bertolusso,
786   B., Thomas, C., Vernet, G., Lynch, J., Moore, N., Cortes, N., Williams, R.,
787   Kidd, S. P., Levett, L. J., Pusok, M., Grant, P. R., Kirk, S., Chatterton, W., Xu-
788   McCrae, L., Smith, D. L., Young, G. R., Bashton, M., Kitchman, K., Gajee, K.,
789   Eastick, K., Lillie, P. J., Burns, P. J., Everson, W., Cox, A., Holmes, A. H.,
790   Bolt, F., Price, J. R., Pond, M., Randell, P. A., Madona, P., Mookerjee, S.,
791   Volz, E. M., Geidelberg, L., Ragonnet-Cronin, M., Boyd, O., Johnson, R.,
792   Pope, C. F., Witney, A. A., Monahan, I. M., Laing, K. G., Smollett, K. L.,
793   McNally, A., McMurray, C., Stockton, J., Quick, J., Loman, N. J., Poplawski,
794   R., Nicholls, S., Rowe, W., Castigador, A., Macnaughton, E., Bouzidi, K. E.,
795   Sudhanva, M., Lampejo, T., Martinez Nunez, R. T., Breen, C., Sluga, G.,
796   Withell, K. T., Machin, N. W., George, R. P., Ahmad, S. S. Y., Pritchard, D. T.,
797   Binns, D., Wong, N., James, V., Williams, C., Illingworth, C. J., Jackson, C.,
798   de Angelis, D., Pascall, D., Mukaddas, A., Broos, A., da Silva Filipe, A., Mair,
799   D., Robertson, D. L., Wright, D. W., Thomson, E. C., Starinskij, I., Tsatsani, I.,
800   Shepherd, J. G., Nichols, J., Hughes, J., Nomikou, K., Tong, L., Orton, R. J.,
801   Vattipally, S., Harvey, W. T., Sanderson, R., O'Brien, S., Rushton, S., Perkins,
802   J., Blacow, R., Gunson, R. N., Gallagher, A., Consortium, P. & The, C.-G. U.
803   K. C. SARS-CoV-2 Omicron is an immune escape variant with an altered cell
804   entry pathway. *Nature Microbiology* **7**, 1161-1179 (2022). 10.1038/s41564-
805   022-01143-7
806
807 42   Saito, A., Irie, T., Suzuki, R., Maemura, T., Nasser, H., Uriu, K., Kosugi, Y.,
808   Shirakawa, K., Sadamasu, K., Kimura, I., Ito, J., Wu, J., Iwatsuki-Horimoto, K.,
809   Ito, M., Yamayoshi, S., Loeber, S., Tsuda, M., Wang, L., Ozono, S.,
810   Butlertanaka, E. P., Tanaka, Y. L., Shimizu, R., Shimizu, K., Yoshimatsu, K.,
811   Kawabata, R., Sakaguchi, T., Tokunaga, K., Yoshida, I., Asakura, H.,
812   Nagashima, M., Kazuma, Y., Nomura, R., Horisawa, Y., Yoshimura, K.,

813 Takaori-Kondo, A., Imai, M., Tanaka, S., Nakagawa, S., Ikeda, T., Fukuhara,
814 T., Kawaoka, Y. & Sato, K. Enhanced fusogenicity and pathogenicity of
815 SARS-CoV-2 Delta P681R mutation. *Nature* **602**, 300-306 (2022).
816 PMC8828475. 10.1038/s41586-021-04266-9

818 43 Rajah, M. M., Hubert, M., Bishop, E., Saunders, N., Robinot, R., Grzelak, L.,
819 Planas, D., Dufloo, J., Gellenoncourt, S., Bongers, A., Zivaljic, M., Planchais,
820 C., Guivel-Benhassine, F., Porrot, F., Mouquet, H., Chakrabarti, L. A.,
821 Buchrieser, J. & Schwartz, O. SARS-CoV-2 Alpha, Beta, and Delta variants
822 display enhanced Spike-mediated syncytia formation. *Embo j* **40**, e108944
823 (2021). PMC8646911. 10.15252/embj.2021108944

825 44 Bowen, J. E., Addetia, A., Dang, H. V., Stewart, C., Brown, J. T., Sharkey, W.
826 K., Sprouse, K. R., Walls, A. C., Mazzitelli, I. G., Logue, J. K., Franko, N. M.,
827 Czudnochowski, N., Powell, A. E., Dellota, E., Jr., Ahmed, K., Ansari, A. S.,
828 Cameroni, E., Gori, A., Bandera, A., Posavad, C. M., Dan, J. M., Zhang, Z.,
829 Weiskopf, D., Sette, A., Crotty, S., Iqbal, N. T., Corti, D., Geffner, J., Snell, G.,
830 Grifantini, R., Chu, H. Y. & Veesler, D. Omicron spike function and
831 neutralizing activity elicited by a comprehensive panel of vaccines. *Science*
832 **377**, 890-894 (2022). PMC9348749. 10.1126/science.abq0203

834 45 Mlcochova, P., Kemp, S. A., Dhar, M. S., Papa, G., Meng, B., Ferreira, I.,
835 Datir, R., Collier, D. A., Albecka, A., Singh, S., Pandey, R., Brown, J., Zhou,
836 J., Goonawardane, N., Mishra, S., Whittaker, C., Mellan, T., Marwal, R.,
837 Datta, M., Sengupta, S., Ponnusamy, K., Radhakrishnan, V. S., Abdullahi, A.,
838 Charles, O., Chattopadhyay, P., Devi, P., Caputo, D., Peacock, T., Wattal, C.,
839 Goel, N., Satwik, A., Vaishya, R., Agarwal, M., Mavousian, A., Lee, J. H.,
840 Bassi, J., Silacci-Fegni, C., Saliba, C., Pinto, D., Irie, T., Yoshida, I., Hamilton,
841 W. L., Sato, K., Bhatt, S., Flaxman, S., James, L. C., Corti, D., Piccoli, L.,
842 Barclay, W. S., Rakshit, P., Agrawal, A. & Gupta, R. K. SARS-CoV-2
843 B.1.617.2 Delta variant replication and immune evasion. *Nature* **599**, 114-119
844 (2021). PMC8566220. 10.1038/s41586-021-03944-y

846 46 Kimura, I., Yamasoba, D., Tamura, T., Nao, N., Suzuki, T., Oda, Y., Mitoma,
847 S., Ito, J., Nasser, H., Zahradnik, J., Uriu, K., Fujita, S., Kosugi, Y., Wang, L.,
848 Tsuda, M., Kishimoto, M., Ito, H., Suzuki, R., Shimizu, R., Begum, M. M.,
849 Yoshimatsu, K., Kimura, K. T., Sasaki, J., Sasaki-Tabata, K., Yamamoto, Y.,
850 Nagamoto, T., Kanamune, J., Kobiyama, K., Asakura, H., Nagashima, M.,
851 Sadamasu, K., Yoshimura, K., Shirakawa, K., Takaori-Kondo, A., Kuramochi,
852 J., Schreiber, G., Ishii, K. J., Hashiguchi, T., Ikeda, T., Saito, A., Fukuhara, T.,
853 Tanaka, S., Matsuno, K. & Sato, K. Virological characteristics of the SARS-
854 CoV-2 Omicron BA.2 subvariants, including BA.4 and BA.5. *Cell* (2022).
855 PMC9472642. 10.1016/j.cell.2022.09.018

857 47 Willett, B. J., Grove, J., MacLean, O. A., Wilkie, C., De Lorenzo, G., Furnon,
858 W., Cantoni, D., Scott, S., Logan, N., Ashraf, S., Manali, M., Szemiel, A.,
859 Cowton, V., Vink, E., Harvey, W. T., Davis, C., Asamaphan, P., Smollett, K.,
860 Tong, L., Orton, R., Hughes, J., Holland, P., Silva, V., Pascall, D. J., Puxty, K.,
861 da Silva Filipe, A., Yebra, G., Shaaban, S., Holden, M. T. G., Pinto, R. M.,
862 Gunson, R., Templeton, K., Murcia, P. R., Patel, A. H., Klenerman, P.,

863   Dunachie, S., Haughney, J., Robertson, D. L., Palmarini, M., Ray, S. &
864   Thomson, E. C. SARS-CoV-2 Omicron is an immune escape variant with an
865   altered cell entry pathway. *Nat Microbiol* **7**, 1161-1179 (2022). PMC9352574
866   COVID-19. The other authors declare no competing interests.
867   10.1038/s41564-022-01143-7
868
869 48   Katsura, H., Sontake, V., Tata, A., Kobayashi, Y., Edwards, C. E., Heaton, B.
870   E., Konkimalla, A., Asakura, T., Mikami, Y., Fritch, E. J., Lee, P. J., Heaton, N.
871   S., Boucher, R. C., Randell, S. H., Baric, R. S. & Tata, P. R. Human Lung
872   Stem Cell-Based Alveolospheres Provide Insights into SARS-CoV-2-Mediated
873   Interferon Responses and Pneumocyte Dysfunction. *Cell Stem Cell* **27**, 890-
874   904.e898 (2020). PMC7577733. 10.1016/j.stem.2020.10.005
875
876 49   Delorey, T. M., Ziegler, C. G. K., Heimberg, G., Normand, R., Yang, Y.,
877   Segerstolpe, Å., Abbondanza, D., Fleming, S. J., Subramanian, A., Montoro,
878   D. T., Jagadeesh, K. A., Dey, K. K., Sen, P., Slyper, M., Pita-Juárez, Y. H.,
879   Phillips, D., Biermann, J., Bloom-Ackermann, Z., Barkas, N., Ganna, A.,
880   Gomez, J., Melms, J. C., Katsyv, I., Normandin, E., Naderi, P., Popov, Y. V.,
881   Raju, S. S., Niezen, S., Tsai, L. T., Siddle, K. J., Sud, M., Tran, V. M.,
882   Vellarikkal, S. K., Wang, Y., Amir-Zilberstein, L., Atri, D. S., Beechem, J.,
883   Brook, O. R., Chen, J., Divakar, P., Dorceus, P., Engreitz, J. M., Essene, A.,
884   Fitzgerald, D. M., Fropf, R., Gazal, S., Gould, J., Grzyb, J., Harvey, T., Hecht,
885   J., Hether, T., Jané-Valbuena, J., Leney-Greene, M., Ma, H., McCabe, C.,
886   McLoughlin, D. E., Miller, E. M., Muus, C., Niemi, M., Padera, R., Pan, L.,
887   Pant, D., Pe'er, C., Pfiffner-Borges, J., Pinto, C. J., Plaisted, J., Reeves, J.,
888   Ross, M., Rudy, M., Rueckert, E. H., Siciliano, M., Sturm, A., Todres, E.,
889   Waghray, A., Warren, S., Zhang, S., Zollinger, D. R., Cosimi, L., Gupta, R. M.,
890   Hacohen, N., Hibshoosh, H., Hide, W., Price, A. L., Rajagopal, J., Tata, P. R.,
891   Riedel, S., Szabo, G., Tickle, T. L., Ellinor, P. T., Hung, D., Sabeti, P. C.,
892   Novak, R., Rogers, R., Ingber, D. E., Jiang, Z. G., Juric, D., Babadi, M., Farhi,
893   S. L., Izar, B., Stone, J. R., Vlachos, I. S., Solomon, I. H., Ashenberg, O.,
894   Porter, C. B. M., Li, B., Shalek, A. K., Villani, A. C., Rozenblatt-Rosen, O. &
895   Regev, A. COVID-19 tissue atlases reveal SARS-CoV-2 pathology and
896   cellular targets. *Nature* **595**, 107-113 (2021). PMC8919505. 10.1038/s41586-
897   021-03570-8
898
899 50   Zhu, N., Wang, W., Liu, Z., Liang, C., Wang, W., Ye, F., Huang, B., Zhao, L.,
900   Wang, H., Zhou, W., Deng, Y., Mao, L., Su, C., Qiang, G., Jiang, T., Zhao, J.,
901   Wu, G., Song, J. & Tan, W. Morphogenesis and cytopathic effect of SARS-
902   CoV-2 infection in human airway epithelial cells. *Nat Commun* **11**, 3910
903   (2020). PMC7413383. 10.1038/s41467-020-17796-z
904
905 51   Li, S., Zhang, Y., Guan, Z., Li, H., Ye, M., Chen, X., Shen, J., Zhou, Y., Shi, Z.
906   L., Zhou, P. & Peng, K. SARS-CoV-2 triggers inflammatory responses and
907   cell death through caspase-8 activation. *Signal Transduct Target Ther* **5**, 235
908   (2020). PMC7545816. 10.1038/s41392-020-00334-0
909
910 52   Ren, Y., Shu, T., Wu, D., Mu, J., Wang, C., Huang, M., Han, Y., Zhang, X. Y.,
911   Zhou, W., Qiu, Y. & Zhou, X. The ORF3a protein of SARS-CoV-2 induces

912   apoptosis in cells. *Cell Mol Immunol* **17**, 881-883 (2020). PMC7301057.
913   10.1038/s41423-020-0485-9
914

915 53 Chan, F. K., Luz, N. F. & Moriwaki, K. Programmed necrosis in the cross talk
916   of cell death and inflammation. *Annu Rev Immunol* **33**, 79-106 (2015).
917   PMC4394030. 10.1146/annurev-immunol-032414-112248
918

919 54 Rock, K. L. & Kono, H. The inflammatory response to cell death. *Annu Rev*
920   *Pathol* **3**, 99-126 (2008). PMC3094097.
921   10.1146/annurev.pathmechdis.3.121806.151456
922

923 55 Zhu, Z., Shi, J., Li, L., Wang, J., Zhao, Y. & Ma, H. Therapy Targets SARS-
924   CoV-2 Infection-Induced Cell Death. *Front Immunol* **13**, 870216 (2022).
925   PMC9152132. 10.3389/fimmu.2022.870216
926

927 56 Karim, F., Gazy, I., Cele, S., Zungu, Y., Krause, R., Bernstein, M., Khan, K.,
928   Ganga, Y., Rodel, H. E., Mthabela, N., Mazibuko, M., Muema, D., Ramjit, D.,
929   Ndung'u, T., Hanekom, W., Gosnell, B., Team, C.-K., Lessells, R. J., Wong, E.
930   B., de Oliveira, T., Moosa, Y., Lustig, G., Leslie, A., Kloverpris, H. & Sigal, A.
931   HIV status alters disease severity and immune cell responses in beta variant
932   SARS-CoV-2 infection wave. *Elife* **10** (2021). 10.7554/eLife.67397
933

934 57 Greaney, A. J., Loes, A. N., Crawford, K. H. D., Starr, T. N., Malone, K. D.,
935   Chu, H. Y. & Bloom, J. D. Comprehensive mapping of mutations in the SARS-
936   CoV-2 receptor-binding domain that affect recognition by polyclonal human
937   plasma antibodies. *Cell Host Microbe* **29**, 463-476.e466 (2021).
938   PMC7869748. 10.1016/j.chom.2021.02.003
939

940 58 Cele, S., Jackson, L., Khoury, D. S., Khan, K., Moyo-Gwete, T., Tegally, H.,
941   San, J. E., Cromer, D., Scheepers, C., Amoako, D. G., Karim, F., Bernstein,
942   M., Lustig, G., Archary, D., Smith, M., Ganga, Y., Jule, Z., Reedoy, K., Hwa,
943   S. H., Giandhari, J., Blackburn, J. M., Gosnell, B. I., Abdool Karim, S. S.,
944   Hanekom, W., von Gottberg, A., Bhiman, J. N., Lessells, R. J., Moosa, M. S.,
945   Davenport, M. P., de Oliveira, T., Moore, P. L. & Sigal, A. Omicron extensively
946   but incompletely escapes Pfizer BNT162b2 neutralization. *Nature* (2021).
947   10.1038/s41586-021-04387-1
948

949 59 Sigal, A., Danon, T., Cohen, A., Milo, R., Geva-Zatorsky, N., Lustig, G., Liron,
950   Y., Alon, U. & Perzov, N. Generation of a fluorescently labeled endogenous
951   protein library in living human cells. *Nat Protoc* **2**, 1515-1527 (2007).
952   10.1038/nprot.2007.197
953

954 60 Jackson, L., Hunter, J., Cele, S., Ferreira, I. M., Young, A. C., Karim, F.,
955   Madansein, R., Dullabh, K. J., Chen, C. Y., Buckels, N. J., Ganga, Y., Khan,
956   K., Boulle, M., Lustig, G., Neher, R. A. & Sigal, A. Incomplete inhibition of HIV
957   infection results in more HIV infected lymph node cells by reducing cell death.
958   *Elife* **7** (2018). PMC5896883. 10.7554/eLife.30134
959

961 61   Sigal, A., Kim, J. T., Balazs, A. B., Dekel, E., Mayo, A., Milo, R. & Baltimore,
962   D. Cell-to-cell spread of HIV permits ongoing replication despite antiretroviral
963   therapy. *Nature* **477**, 95-98 (2011). 10.1038/nature10347

964 62   Ko, S. H., Bayat Mokhtari, E., Mudvari, P., Stein, S., Stringham, C. D.,
965   Wagner, D., Ramelli, S., Ramos-Benitez, M. J., Strich, J. R., Davey, R. T., Jr.,
966   Zhou, T., Misasi, J., Kwong, P. D., Chertow, D. S., Sullivan, N. J. & Boritz, E.
967   A. High-throughput, single-copy sequencing reveals SARS-CoV-2 spike
968   variants coincident with mounting humoral immunity during acute COVID-19.
969   *PLoS Pathog* **17**, e1009431 (2021). PMC8031304.
970   10.1371/journal.ppat.1009431

972 63   Jackson, L., Rodel, H., Hwa, S.-H., Cele, S., Ganga, Y., Tegally, H.,
973   Bernstein, M., Giandhari, J., Gosnell, B. I., Khan, K., Hanekom, W., Karim, F.,
974   de Oliveira, T., Moosa, M.-Y. S. & Sigal, A. SARS-CoV-2 cell-to-cell spread
975   occurs rapidly and is insensitive to antibody neutralization. *bioRxiv*,
976   2021.2006.2001.446516 (2021). 10.1101/2021.06.01.446516

978 64   Rajah, M. M., Bernier, A., Buchrieser, J. & Schwartz, O. The Mechanism and
979   Consequences of SARS-CoV-2 Spike-Mediated Fusion and Syncytia
980   Formation. *J Mol Biol* **434**, 167280 (2022). PMC8485708.
981   10.1016/j.jmb.2021.167280

983 65   Mlcochova, P., Kemp, S., Dhar, M. S., Papa, G., Meng, B., Ferreira, I., Datir,
984   R., Collier, D. A., Albecka, A., Singh, S., Pandey, R., Brown, J., Zhou, J.,
985   Goonawardane, N., Mishra, S., Whittaker, C., Mellan, T., Marwal, R., Datta,
986   M., Sengupta, S., Ponnusamy, K., Radhakrishnan, V. S., Abdullahi, A.,
987   Charles, O., Chattopadhyay, P., Devi, P., Caputo, D., Peacock, T., Wattal, D.
988   C., Goel, N., Satwik, A., Vaishya, R., Agarwal, M., Indian, S.-C.-G. C.,
989   Genotype to Phenotype Japan, C., Collaboration, C.-N. B. C.-., Mavousian,
990   A., Lee, J. H., Bassi, J., Silacci-Fegni, C., Saliba, C., Pinto, D., Irie, T.,
991   Yoshida, I., Hamilton, W. L., Sato, K., Bhatt, S., Flaxman, S., James, L. C.,
992   Corti, D., Piccoli, L., Barclay, W. S., Rakshit, P., Agrawal, A. & Gupta, R. K.
993   SARS-CoV-2 B.1.617.2 Delta variant replication and immune evasion. *Nature*
994   (2021). 10.1038/s41586-021-03944-y

996 66   Nardacci, R., Perfettini, J. L., Grieco, L., Thieffry, D., Kroemer, G. &
997   Piacentini, M. Syncytial apoptosis signaling network induced by the HIV-1
998   envelope glycoprotein complex: an overview. *Cell Death Dis* **6**, e1846 (2015).
999   PMC4558497. 10.1038/cddis.2015.204

1001 67   Wolter, N., Jassat, W., Walaza, S., Welch, R., Moultrie, H., Groome, M.,
1002   Amoako, D. G., Everatt, J., Bhiman, J. N., Scheepers, C., Tebeila, N.,
1003   Chiwandire, N., du Plessis, M., Govender, N., Ismail, A., Glass, A., Mlisana,
1004   K., Stevens, W., Treurnicht, F. K., Makatini, Z., Hsiao, N. Y., Parboosing, R.,
1005   Wadula, J., Hussey, H., Davies, M. A., Boulle, A., von Gottberg, A. & Cohen,
1006   C. Early assessment of the clinical severity of the SARS-CoV-2 omicron
1007   variant in South Africa: a data linkage study. *Lancet* **399**, 437-446 (2022).
1008   PMC8769664 Medical Research Council, the UK Foreign, Commonwealth
1009   and Development Office, the Wellcome Trust, the US Centers for Disease

24

1021

1022 68   Khan, K., Karim, F., Cele, S., Reedoy, K., San, J. E., Lustig, G., Tegally, H.,
1023   Rosenberg, Y., Bernstein, M., Jule, Z., Ganga, Y., Ngcobo, N., Mazibuko, M.,
1024   Mthabela, N., Mhlane, Z., Mbatha, N., Miya, Y., Giandhari, J., Ramphal, Y.,
1025   Naidoo, T., Sivro, A., Samsunder, N., Kharsany, A. B. M., Amoako, D.,
1026   Bhiman, J. N., Manickchund, N., Karim, Q. A., Magula, N., Abdool Karim, S.
1027   S., Gray, G., Hanekom, W., von Gottberg, A., Milo, R., Gosnell, B. I., Lessells,
1028   R. J., Moore, P. L., de Olveira, T., Moosa, M. S. & Sigal, A. Omicron infection
1029   enhances Delta antibody immunity in vaccinated persons. *Nature* (2022).
1030   10.1038/s41586-022-04830-x

1031

1032 69   Cele, S., Gazy, I., Jackson, L., Hwa, S. H., Tegally, H., Lustig, G., Giandhari,
1033   J., Pillay, S., Wilkinson, E., Naidoo, Y., Karim, F., Ganga, Y., Khan, K.,
1034   Bernstein, M., Balazs, A. B., Gosnell, B. I., Hanekom, W., Moosa, M. S.,
1035   Network for Genomic Surveillance in South, A., Team, C.-K., Lessells, R. J.,
1036   de Oliveira, T. & Sigal, A. Escape of SARS-CoV-2 501Y.V2 from
1037   neutralization by convalescent plasma. *Nature* **593**, 142-146 (2021).
1038   10.1038/s41586-021-03471-w

1039

1040

1041

Figure legends

Figure 1: Evolution of SARS-CoV-2 from ancestral virus in an immunosuppressed individual. (**A**) SARS-CoV-2 qPCR cycle threshold (Ct) values over time. Each point represents a study visit and visits at which D6 and D190 viruses were isolated are marked with purple and orange points, respectively. Horizontal red line denotes threshold of detection. (**B**) Neutralization of D6 and D190 isolates by convalescent participant plasma with immunity elicited by D614G (left), Beta (middle) or Delta (right) variant infection. Per participant fold-drop was calculated by dividing infecting virus neutralization, quantified as $FRNT_{50}$, by D6 or D190 neutralization. Bars represent geometric means of fold-change per participant group. p-values were **p=0.003, ****p<0.0001 by the Wilcoxon Rank Sum test. (**C**) Phylogenetic analysis of the infection, with isolates from the evolving infection tested in this study shown in red. (**D**) Substitutions and deletions in D6, D20, D34, D106, and D190 isolates relative to ancestral virus.

Figure 2: Changes in infection induced cell fusion and cell number. (**A**) Representative transmitted light (first row), nuclear YFP fluorescence (second row), and overlay images (third row) of infected cells from time-lapse imaging. Red in the overlay image denotes automated detection of nuclear area. Time of image post-infection is top right as hours:minutes. Scale bar is 50 μm. (**B**) Fraction of fused cells and (**C**) fold-change in cell number over time post-movie start, where infection is at the start of the movie. Lines and shaded areas are medians and 95% confidence intervals of 3-6 independent time-lapse experiments, with each experiment containing 12 fields of view per infection condition. Infection conditions were uninfected (green), Omicron BA.1 (grey), D6 (purple), D190 (orange) or ancestral D614G (blue) infection.

Figure 2 – figure supplement 1: Overview of automated image analysis. Images of fluorescently labelled nuclei were loaded to MATLAB 2019b and a binary mask was generated by thresholding on the fluorescent signal to separate individual objects. An object was classified as multinucleate/fused (red) if the object's area was larger than the maximum determined size for a single nucleus, and uni-nucleate (green) otherwise. The maximum size threshold for a single nucleus was calculated as the mean nuclear area of uninfected cells at 12 hours post-movie start plus 3 standard deviations of the mean. The total number of nuclei per movie frame was determined by dividing the sum of the nuclear area by the mean area of a single nucleus, and the fraction of fused cells was determined by dividing the sum of the area of nuclei scored as fused by the sum of the total nuclear area.

26

1078

1079 **Figure 2 – figure supplement 2: Fold-change in cell number post-infection with**

1080 **exclusion of fused cells.** Fold-change in cell number over time post-movie start. Total

1081 number of unfused cells was determined by subtracting the total area of fused nuclei from

1082 the sum of the total area occupied by nuclei, then dividing the remaining nuclear area by the

1083 mean area of a single nucleus. Lines and shaded areas are median and 95% confidence

1084 intervals of 3-6 independent time-lapse experiments containing 12 fields of view each per

1085 infection condition. Infection conditions were uninfected (green), BA.1 (grey), D6 (purple),

1086 D190 (orange) or ancestral D614G (blue).

1087

1088 **Figure 3: Infection by SARS-CoV-2 isolated at different times during long-term**

1089 **infection results in different levels of cell death.** (**A**) Flow cytometry gating strategy. First

1090 panel shows uninfected cells, second panel shows 80% ethanol-treated cells (positive

1091 control), and third and fourth panels show live infected cells (green gate) and dead infected

1092 cells (red gate) 24 hours post-infection with D614G and Omicron BA.1. Numbers represent

1093 percentages of cells in the corresponding quadrants. (**B**) Fraction of dead cells 24 hours

1094 post-infection in infections by D190, Omicron subvariants BA.1 and BA.5, and two

1095 independent isolates of ancestral virus with the D614G substitution. (**C**) Fraction of dead

1096 cells 24 hours post-infection in infections by D190, D106, D34, D20, and D6. Horizontal bars

1097 represent medians with interquartile ranges of 10-22 replicates from 3-8 independent

1098 experiments with all experiments containing D190 and the D614G isolate 1 for reference. p-

1099 values were determined by the Kruskal-Wallis test with Dunn multiple comparisons

1100 correction, with all comparisons to D190. Significant p-values were ***p=0.0001 (D190 vs.

1101 BA.1), **p=0.0015 (D190 vs. BA.5), ****p< 0.0001 (D190 vs. D6) and **p=0.0064 (D190 vs.

1102 D20).

1103

1104 **Figure 4: Changes in spike cell surface expression during evolution.** (**A**) Expression of

1105 spike (left 2 wells) and nucleocapsid (right 2 wells) in representative infection foci formed by

1106 ancestral virus at 18 hours post-infection. For each set of two images, the cells in the left

1107 image were stained without permeabilization and show cell surface expression of either

1108 spike or nucleocapsid. The cells on the right have been permeabilized and show both

1109 surface and intracellular spike or nucleocapsid expression. Each image represents the

1110 complete area of one well of a 96-well plate in a live virus focus forming assay. Bar is 2 mm.

1111 (**B**) The mean intensity of surface spike levels of individual foci, normalized per experiment

1112 to the mean of the ancestral virus cell surface spike expression obtained in the experiment.

1113 Mean intensity data from 2038 (D190), 1913 (D6), 1627 (BA.1), 1237 (BA.5), 1028 (D614G

1114 isolate 2), and 3052 (D614G isolate 1) foci from 3-6 independent experiments. p-values were

27

1115   determined by the Kruskal-Wallis test with Dunn multiple comparisons correction, with all

1116   comparisons to D190 and all ****$p<0.0001$.

1117

1118   **Video captions**

1119

1120   **Video 1:** Representative field of view of uninfected H1299-ACE2 cells over 50 hours of

1121   imaging at 10-minute intervals between frames.

1122

1123   **Video 2:** Representative field of view of ancestral D614G virus infected H1299-ACE2 cells

1124   over 50 hours of imaging at 10-minute intervals between frames.

1125

1126   **Video 3:** Representative field of view of Omicron BA.1 virus infected H1299-ACE2 cells over

1127   50 hours of imaging at 10-minute intervals between frames.

1128

1129   **Video 4:** Representative field of view of D6 isolate virus infected H1299-ACE2 cells over 50

1130   hours of imaging at 10-minute intervals between frames.

1131

1132   **Video 5:** Representative field of view of D190 isolate virus infected H1299-ACE2 cells over

1133   50 hours of imaging at 10-minute intervals between frames.
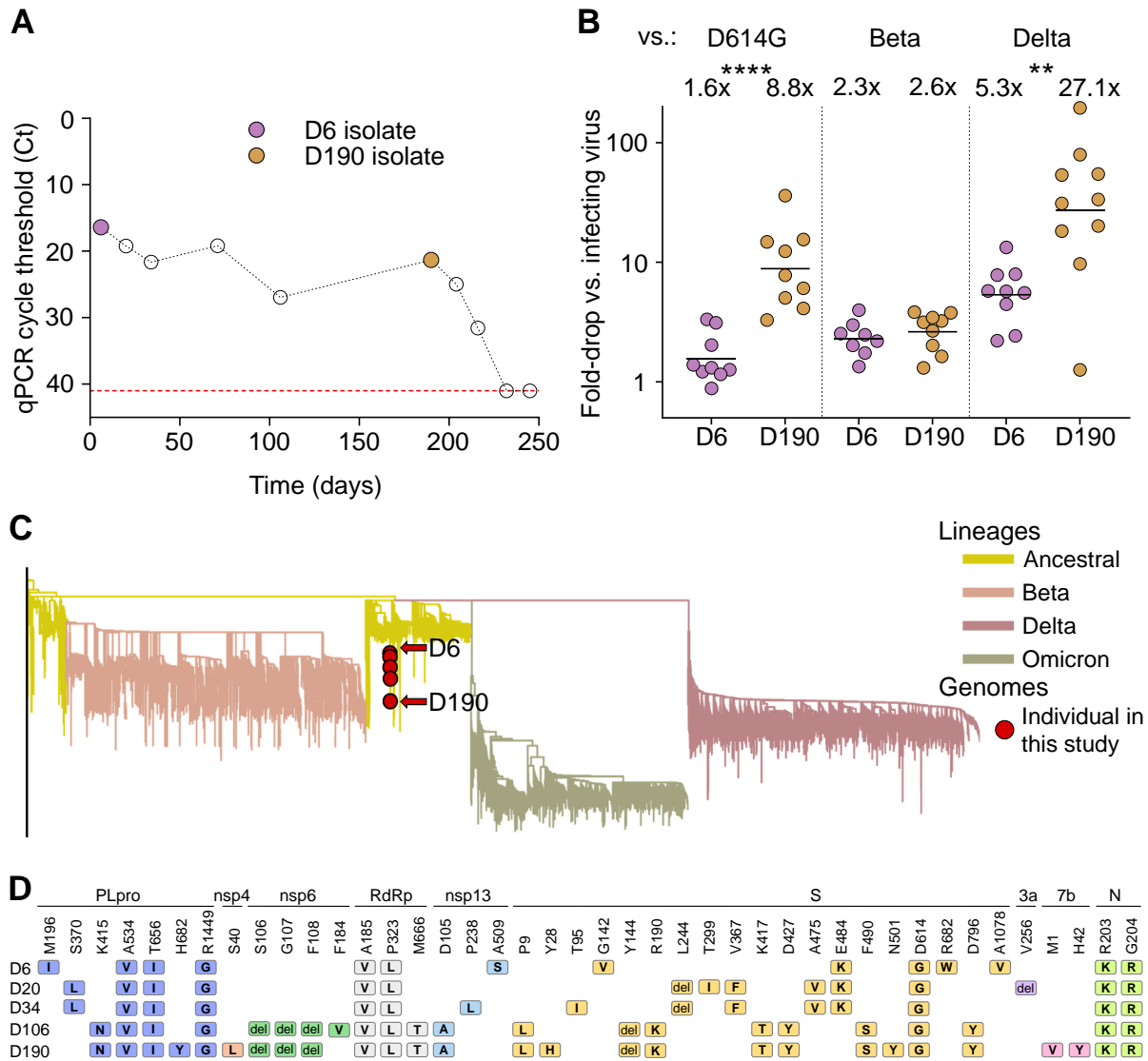
Figure 1: **Evolution of SARS-CoV-2 from ancestral virus in an immunosuppressed individual.** (A) SARS-CoV-2 qPCR cycle threshold (Ct) values over time. Each point represents a study visit and visits at which D6 and D190 viruses were isolated are marked with purple and orange points, respectively. Horizontal red line denotes threshold of detection. (B) Neutralization of D6 and D190 isolates by convalescent participant plasma with immunity elicited by D614G (left), Beta (middle) or Delta (right) variant infection. Per participant fold-drop was calculated by dividing infecting virus neutralization, quantified as $FRNT_{50}$, by D6 or D190 neutralization. Bars represent geometric means of fold-change per participant group. p-values were **p=0.003, ****p<0.0001 by the Wilcoxon Rank Sum test. (C) Phylogenetic analysis of the infection, with isolates from the evolving infection tested in this study shown in red. (D) Substitutions and deletions in D6, D20, D34, D106, and D190 isolates relative to ancestral virus.
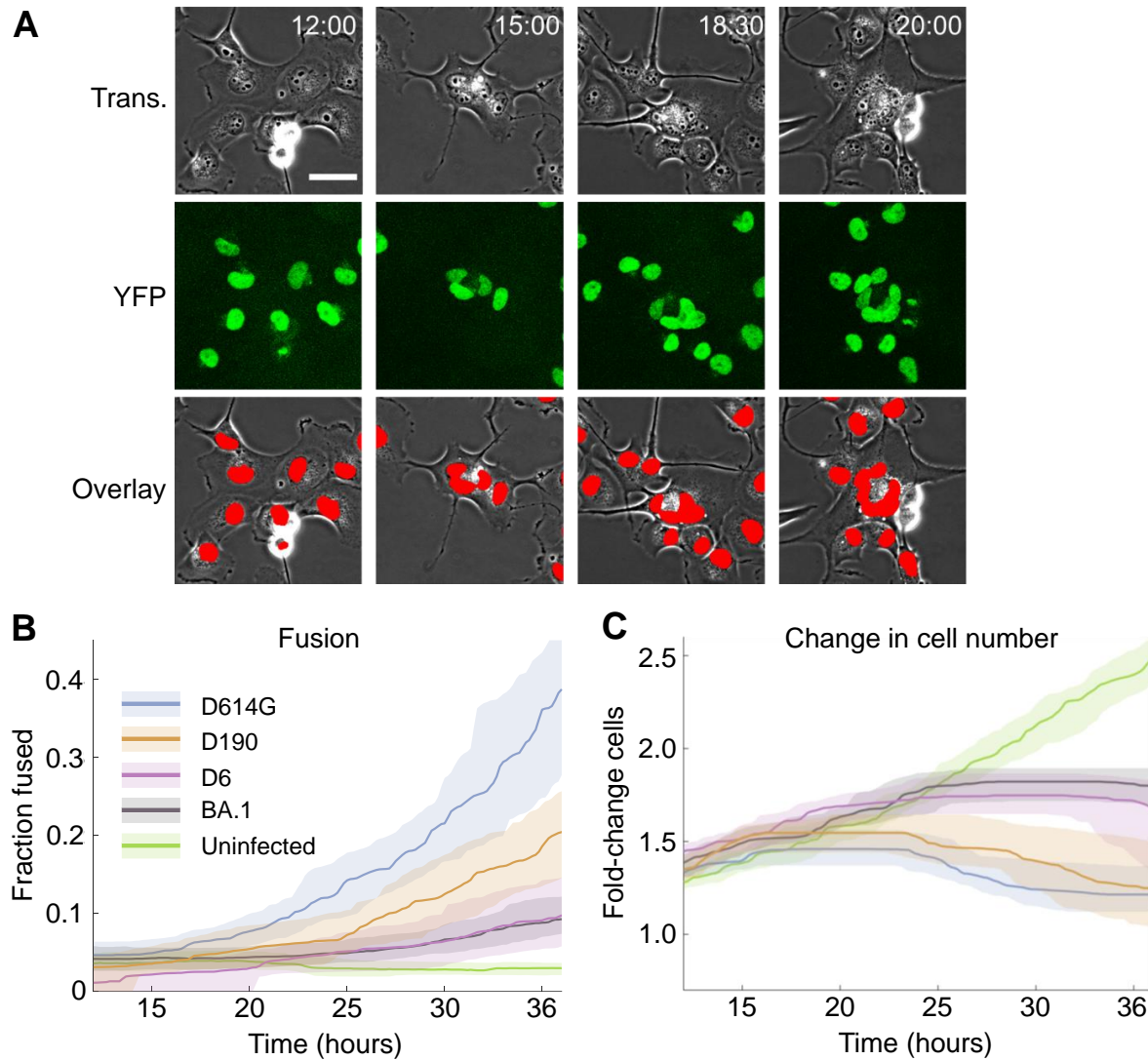
Figure 2: Changes in infection induced cell fusion and cell number. (A) Representative transmitted light (first row), nuclear YFP fluorescence (second row), and overlay images (third row) of infected cells from time-lapse imaging. Red in the overlay image denotes automated detection of nuclear area. Time of image post-infection is top right as hours:minutes. Scale bar is 50 μm. (B) Fraction of fused cells and (C) fold-change in cell number over time post-movie start, where infection is at the start of the movie. Lines and shaded areas are medians and 95% confidence intervals of 3-6 independent time-lapse experiments, with each experiment containing 12 fields of view per infection condition. Infection conditions were uninfected (green), Omicron BA.1 (grey), D6 (purple), D190 (orange) or ancestral D614G (blue) infection.
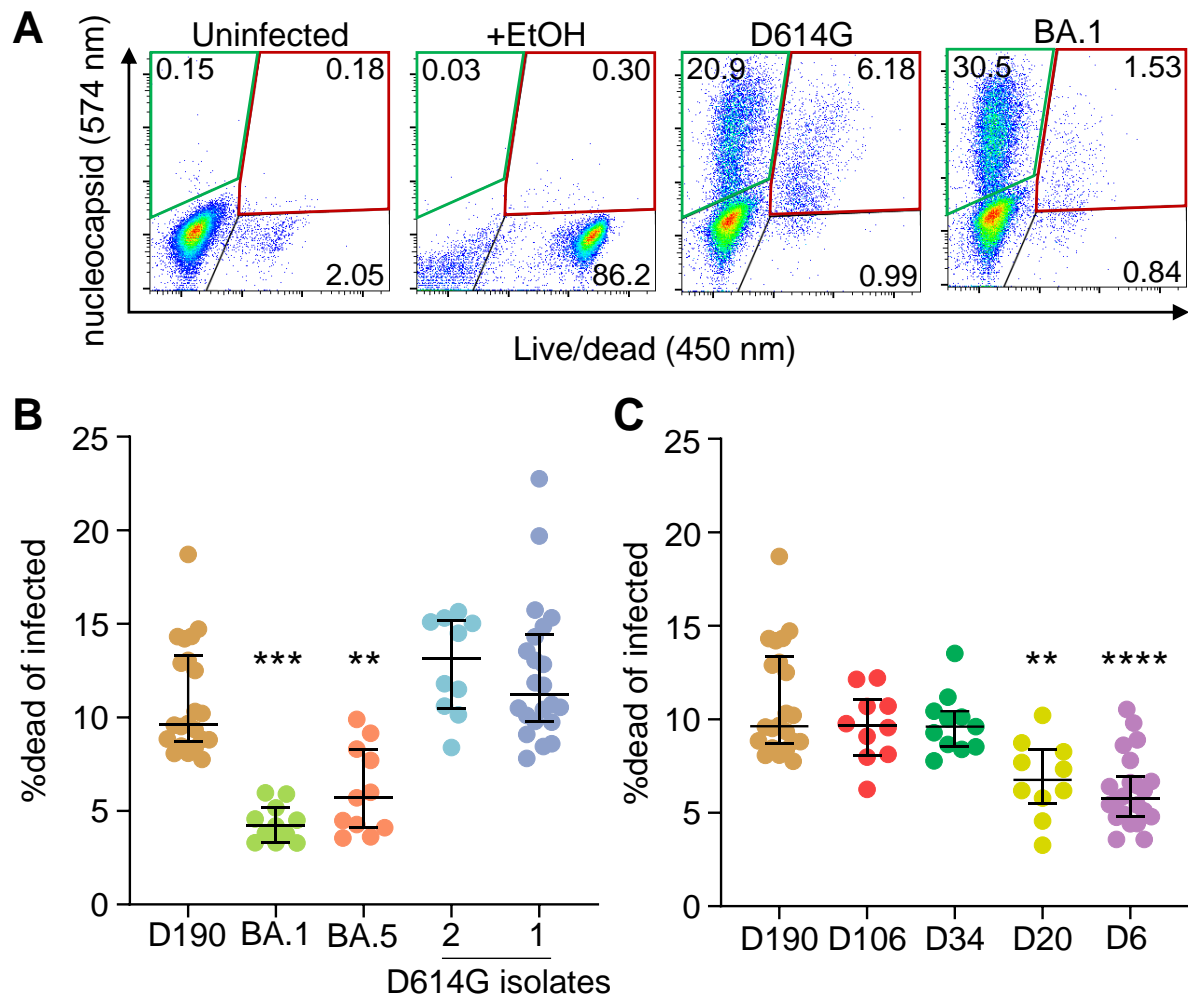
Figure 3: Infection by SARS-CoV-2 isolated at different times during long-term infection results in different levels of cell death. (A) Flow cytometry gating strategy. First panel shows uninfected cells, second panel shows 80% ethanol-treated cells (positive control), and third and fourth panels show live infected cells (green gate) and dead infected cells (red gate) 24 hours post-infection with D614G and Omicron BA.1. Numbers represent percentages of cells in the corresponding quadrants. (B) Fraction of dead cells 24 hours post-infection in infections by D190, Omicron subvariants BA.1 and BA.5, and two independent isolates of ancestral virus with the D614G substitution. (C) Fraction of dead cells 24 hours post-infection in infections by D190, D106, D34, D20, and D6. Horizontal bars represent medians with interquartile ranges of 10-22 replicates from 3-8 independent experiments with all experiments containing D190 and the D614G isolate 1 for reference. p-values were determined by the Kruskal-Wallis test with Dunn multiple comparisons correction, with all comparisons to D190. Significant p-values were ***p=0.0001 (D190 vs. BA.1), **p=0.0015 (D190 vs. BA.5), ****p< 0.0001 (D190 vs. D6) and **p=0.0064 (D190 vs. D20).
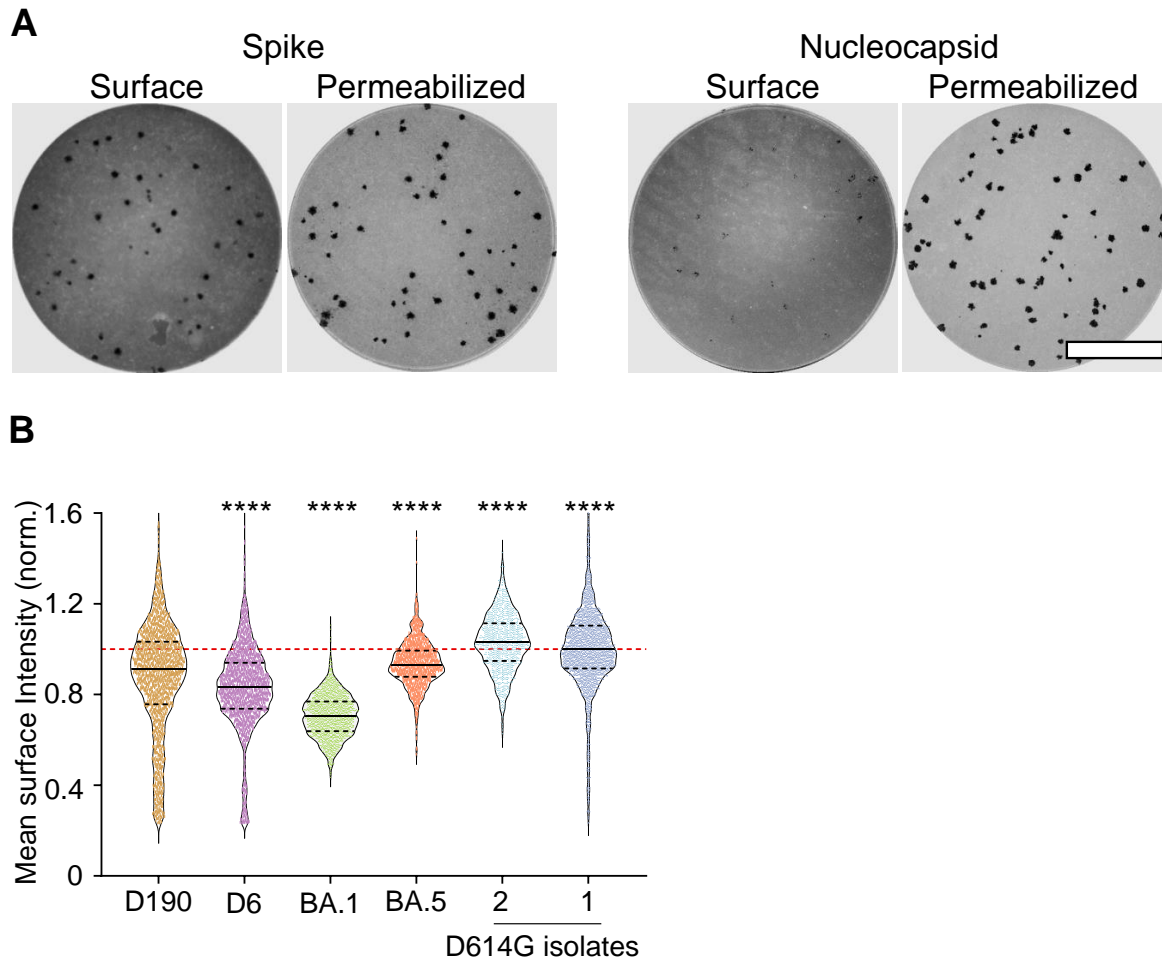
Figure 4: Changes in spike cell surface expression during evolution. (A) Expression of spike (left 2 wells) and nucleocapsid (right 2 wells) in representative infection foci formed by ancestral virus at 18 hours post-infection. For each set of two images, the cells in the left image were stained without permeabilization and show cell surface expression of either spike or nucleocapsid. The cells on the right have been permeabilized and show both surface and intracellular spike or nucleocapsid expression. Each image represents the complete area of one well of a 96-well plate in a live virus focus forming assay. Bar is 2 mm. (B) The mean intensity of surface spike levels of individual foci, normalized per experiment to the mean of the ancestral virus cell surface spike expression obtained in the experiment. Mean intensity data from 2038 (D190), 1913 (D6), 1627 (BA.1), 1237 (BA.5), 1028 (D614G isolate 2), and 3052 (D614G isolate 1) foci from 3-6 independent experiments. p-values were determined by the Kruskal-Wallis test with Dunn multiple comparisons correction, with all comparisons to D190 and all ****p<0.0001.
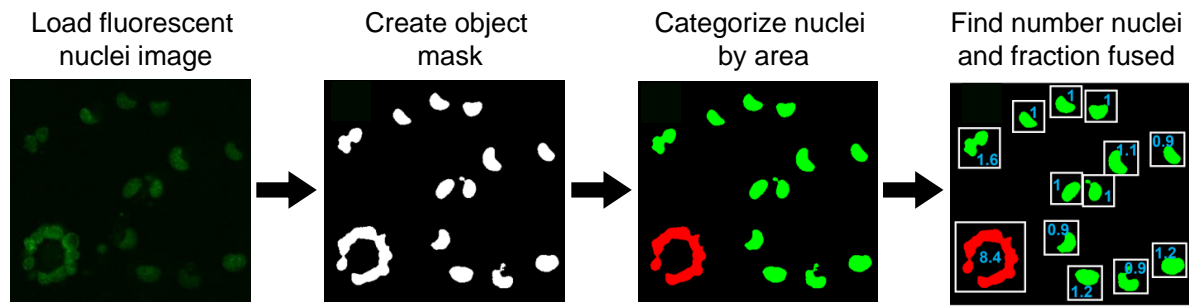
Figure 2 - figure supplement 1: Overview of automated image analysis. Images of fluorescently labelled nuclei were loaded to MATLAB 2019b and a binary mask was generated by thresholding on the fluorescent signal to separate individual objects. An object was classified as multinucleate/fused (red) if the object's area was larger than the maximum determined size for a single nucleus, and uni-nucleate (green) otherwise. The maximum size threshold for a single nucleus was calculated as the mean nuclear area of uninfected cells at 12 hours post-movie start plus 3 standard deviations of the mean. The total number of nuclei per movie frame was determined by dividing the sum of the nuclear area by the mean area of a single nucleus, and the fraction of fused cells was determined by dividing the sum of the area of nuclei scored as fused by the sum of the total nuclear area.
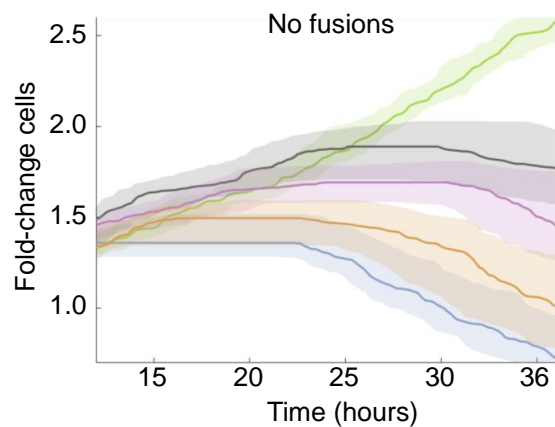

Figure 2 - figure supplement 2: Fold-change in cell number post-infection with exclusion of fused cells. Fold-change in cell number over time post-movie start. Total number of unfused cells was determined by subtracting the total area of fused nuclei from the sum of the total area occupied by nuclei, then dividing the remaining nuclear area by the mean area of a single nucleus. Lines and shaded areas are median and 95% confidence intervals of 3-6 independent time-lapse experiments containing 12 fields of view each per infection condition. Infection conditions were uninfected (green), BA.1 (grey), D6 (purple), D190 (orange) or ancestral D614G (blue).